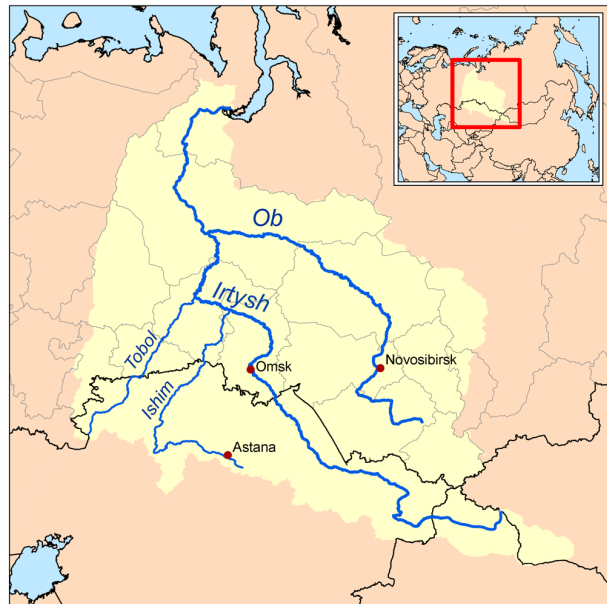


Understanding the positive trend in total water storage of Ob river basin using spaceborn observation



Bachelorarbeit im Studiengang
Geodäsie und Geoinformatik
an der Universität Stuttgart

Ziqing Yu

Stuttgart, November 2020

Supervisor: Dr.-Ing. Mohammad Tourian
Universität Stuttgart

M.Sc. Peyman Saemian
Universität Stuttgart

Erklärung der Urheberschaft

Ich erkläre hiermit an Eides statt, dass ich die vorliegende Arbeit ohne Hilfe Dritter und ohne Benutzung anderer als der angegebenen Hilfsmittel angefertigt habe; die aus fremden Quellen direkt oder indirekt übernommenen Gedanken sind als solche kenntlich gemacht. Die Arbeit wurde bisher in gleicher oder ähnlicher Form in keiner anderen Prüfungsbehörde vorgelegt und auch noch nicht veröffentlicht.

Ort, Datum

Unterschrift

In recent years, a positive trend of total water storage is detected in many big basins. One of them is Ob river basin in west Siberia. In this thesis, measurements from GRACE and GRACE-FO mission are employed and analyzed to determine the total water storage change in this region. Meanwhile, precipitation and evapotranspiration from global datasets and runoff determined using satellite altimetry will also be taken into discussion. Finally, those questions will be answered: how did the total water storage change from January of 2003 to December of 2019? In which period did these changes happen and what are the reasons behind them?

Contents

1	Introduction	1
1.1	Water Cycle	1
1.1.1	Precipitation	1
1.1.2	Evapotranspiration	2
1.1.3	Runoff	3
1.2	Observation from satellite gravimetry	3
1.3	Motivation	5
2	Study Area	7
2.1	Physiography	8
2.2	Climate	8
2.3	Hydrology	9
2.4	Permafrost	9
2.5	Human use	10
3	Data	11
3.1	GRACE and GRACE-FO	11
3.1.1	Spherical harmonics	11
3.1.2	Mass concentration	11
3.2	Precipitation	13
3.3	Evapotranspiration	15
3.4	Runoff	16
3.4.1	Global datasets	16
3.4.2	Water level height	16
4	Method	21
4.1	Estimating hydrological component from datasets	21
4.1.1	Adjustment using Gauss-Markov model	22
4.2	Estimating the quality of runoff datasets	24
4.3	Estimating the runoff using quantile function and water level	24
5	Result	27
5.1	Total water storage	27
5.2	Precipitation	29
5.3	Evapotranspiration	30
5.4	Runoff	32
5.4.1	Runoff from global datasets	32
5.4.2	Estimating runoff using quantile function and satellite altimetry	33
5.5	Discussion about the quality	36

6 Conclusion and outlook	37
6.1 Conclusion	37
6.2 Outlook	37
A Estimating TWS from GRACE SH	XV

List of Figures

1.1	hydrologic cycle https://www.usgs.gov/special-topic/water-science-school/science/water-cycle-adults-and-advanced-students	2
1.2	GRACE Component [15]	4
1.3	GRACE-FO twin satellites https://space.skyrocket.de/doc_sdat/grace-fo.htm	5
1.4	Trends in TWS (in centimetres per year) obtained on the basis of GRACE observations from April 2002 to March 2016. The cause of the trend in each outlined study region is briefly explained and colour-coded by category. The trend map was smoothed with a 150 km radius Gaussian filter for the purpose of visualization; however, all calculations were performed at the native 3° resolution of the data product. the figure is adapted from [19]	6
1.5	Total water storage change from Jan. 2003 to Dec. 2019 in Ob river basin from mascon CSR RL06	6
2.1	River Basins Ob http://www.geologypage.com/2014/03/ob-river.html	7
2.2	Asia Map of Koeppen-Geiger climate classification [17]	9
3.1	The distribution of 40,962 geodesic grid tiles over the Earth used as a basis function for estimation of mass anomalies from GRACE for CSR mascon solutions. (top) Global view, (bottom left) South Pole view, and (bottom right) North Pole view [20]	12
3.2	Station Salekhard	17
4.1	Available in-situ runoff for Ob river (top left), stimatEd water level from Envisat (top right), and quantile function of water level and runoff (middle). A smoothened rating curve is obtained from the corresponding probabilities (bottom)	25
5.1	TWSA generated from different data centers (top) generate one summarized TWSA time series (bottom) from Jan.2003 to Dec.2019	27
5.2	the derivation of TWSA (top) and the abrupt change in the moving average (bottom)	28
5.3	mean value with uncertainty of dS/dt and RMSE in 3 periods	28
5.4	spatial TWS change of Ob river basin in each period using mascon CSR RL06 solution	29
5.5	all precipitation datasets (top) are summarized into one time series, the mean precipitation with RMSE in 3 periods are calculated (bottom)	29
5.6	spatial change of precipitation in Ob river basin using different datasets in June of 2003	30
5.7	all evapotranspiration datasets (top) are summarized into one time series, the mean precipitation with uncertainty in 3 periods are calculated (bottom)	31

5.8	spatial change of evapotranspiration in Ob river basin using different datasets in June of 2003	31
5.9	Runoff datasets, the black bold time series is the in-situ runoff	32
5.10	CDF of differences	33
5.11	water level time series and the location of virtual station for different space mission	34
5.12	runoff timeseries calculated from water level (top) and the mean value in 3 periods, the red points are unusually high and to be ignored(bottom)	35
5.13	runoff time series and mean value in 3 periods after 2 unusual months are ignored	35

List of Tables

3.1	precipitation datasets	13
3.2	evapotranspiration datasets	15
3.3	runoff datasets	17
5.1	RMSE for runoff datacenters	32
5.2	mean value of all water cycle component in 3 periods with uncertainties	36

Chapter 1

Introduction

1.1 Water Cycle

Water is one of the most important ingredient of life; it regulates climate and many industries need water as coolant, solvent, rea material, etc. Water covers about 71% of the earth's surface. However, 98 % of the water on the earth is in the oceans, 1.6% is in ice caps, which means only 0.4 % is the fresh water on land [8]. The water on earth is variable depending on a wide range of climatic variables. A very little variability of the hydrology cycle can have big effects on water resources. [6]

The hydrology cycle (Figure 1.1) includes 3 major compartments: precipitation, evapo-transpiration and runoff. The water evaporates from the oceans and the land surface as vapor to become part of the atmosphere along with water from evapotranspiration

Evapotranspiration, which is water transpired from plants and evaporated from the soil and the cooler temperature causes the vapor into clouds. The clouds fall out of the sky as precipitation, which includes rain, snow and ice. Most precipitation falls back into the oceans or onto land. Precipitated water may be intercepted by vegetation, become overland flow over the ground surface, flow through the soil as subsurface flow and discharge into streams as surface runoff. The process can be simplified as:

$$P - ET - R = \frac{dS}{dt} \quad (1.1)$$

where

P	Precipitation
ET	Evapotranspiration
R	Surface Runoff
dS/dt	total water storage change

1.1.1 Precipitation

Precipitation is any form of water particle, solid or liquid, that falls from the atmosphere and reaches the ground. Precipitation can include drizzle, rain, snow, sleet, and hail. Precipitation forms in the clouds when water vapor condenses into bigger and bigger droplets of water.

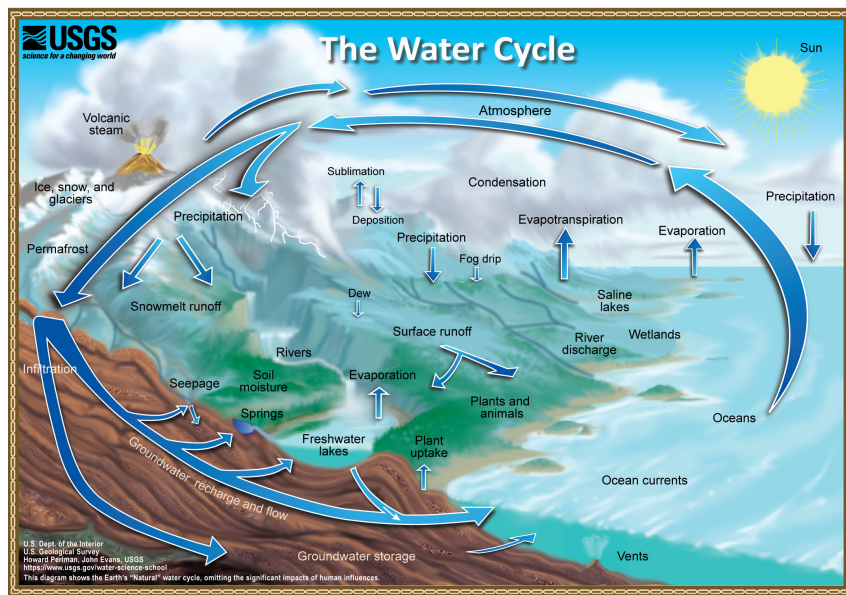


Figure 1.1: hydrologic cycle <https://www.usgs.gov/special-topic/water-science-school/science/water-cycle-adults-and-advanced-students>

When the drops are heavy enough, they fall to the Earth. If a cloud is colder, like it would be at higher altitudes, the water droplets may freeze to form ice. These ice crystals then fall to the Earth as snow, hail, or rain, depending on the temperature within the cloud and at the Earth's surface. Most rain actually begins as snow high in the clouds. As the snowflakes fall through warmer air, they become raindrops.

Precipitation is responsible for depositing the fresh water on the planet. Approximately 505 000 cubic kilometres of water falls as precipitation each year; 398 000 cubic kilometres of it over the oceans and 107 000 cubic kilometres over land.[5] Given the Earth's surface area, that means the globally averaged annual precipitation is 990 millimetres , but over land it is only 715 millimetres

1.1.2 Evapotranspiration

Evaporation and transpiration occur simultaneously and there is no easy way of distinguishing between the two processes.[2]. Evaporation is the process whereby liquid water is converted to water vapour and removed from the evaporating surface. Water evaporates from a variety of surfaces, such as lakes, rivers, pavements, soils and wet vegetation. Transpiration consists of the vaporization of liquid water contained in plant tissues and the vapour removal to the atmosphere. Crops predominately lose their water through stomata. These are small openings on the plant leaf through which gases and water vapour pass. The water, together with some nutrients, is taken up by the roots and transported through the plant. The vaporization occurs within the leaf, namely in the intercellular spaces, and the vapour exchange with the atmosphere is controlled by the stomatal aperture. Nearly all water taken up is lost by transpiration and only a tiny fraction is used within the plant.[16]

1.1.3 Runoff

Runoff is quantity of water discharged in surface streams. Runoff includes not only the waters that travel over the land surface and through channels to reach a stream but also interflow, the water that infiltrates the soil surface and travels by means of gravity toward a stream channel (always above the main groundwater level) and eventually empties into the channel. Runoff also includes groundwater that is discharged into a stream; streamflow that is composed entirely of groundwater is termed base flow, or fair-weather runoff, and it occurs where a stream channel intersects the water table.

1.2 Observation from satellite gravimetry

Unlike many water cycle phenomena like precipitation, ground-based measurement of total water storage is quite a challenge. In some way, remote sensing with satellite is the perfect tool for hydrology research, which has the ability to provide the data globally in a long term.

The GRACE mission is a joint partnership between the National Aeronautics and Space Administration (NASA) in the United States, the Deutsche Forshungsanstalt fuer Luft und Raumfahrt (DLR) in Germany. The Grace Satellites launched on 17 March 2002, are making detailed measurements of Earth's gravity field, which are caused by monthly changes in mass. [22] The mass changes can be thought of as concentrated in a very thin layer of water thickness changes near the Earth's surface by moving ocean, atmospheric and land ice masses and by mass exchanges between these Earth system compartments.[1]

The two identical satellites orbit one behind the other in the same orbital plane at an approximate distance of 220 km (137 miles). As the pair circles the Earth, areas of slightly stronger gravity (greater mass concentration) will affect the lead satellite first, pulling it away from the trailing satellite, then as the satellites continue along their orbital path, the trailing satellite is pulled toward the lead satellite as it passes over the gravity anomaly. The change in distance would certainly be imperceptible to our eyes, but an extremely precise microwave ranging system on GRACE is able to detect these minuscule changes in the distance between the satellites. A highly accurate measuring device known as an accelerometer, located at each satellite mass center, will be used to measure the non-gravitational accelerations (such as those due to atmospheric drag) so that only accelerations caused by gravity are considered. Satellite Global Positioning System (GPS) receivers will be used to determine the exact position of the satellite over the Earth to within a centimeter or less. Members of the GRACE science team can download all this information from the satellites, and use it to construct monthly maps of the Earth's average gravity field.

The component parts of GRACE: (Figure 1.2) [15]

- K-band Ranging System (KBR): Provides precise (within 10 micrometre) measurements of the distance change between the two satellites needed to measure fluctuations in gravity.
- Ultra Stable Oscillator (USO): Provides frequency generation for the K-band ranging system.

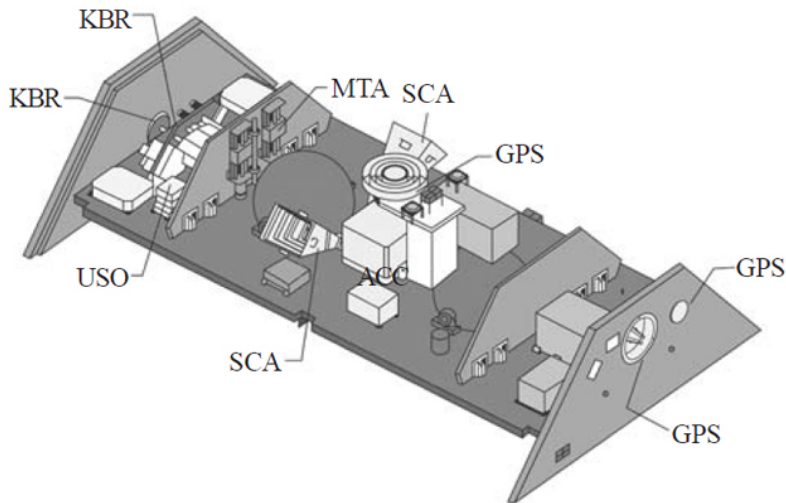


Figure 1.2: GRACE Component [15]

- SuperSTAR Accelerometers (ACC): Precisely measures the non-gravitational accelerations acting on the satellites.
- Star Camera Assembly (SCA): Precisely determines the two satellite's orientation by tracking them relative to the position of the stars.
- Coarse Earth Sun and Sensor (CES): Provides omnidirectional, reliable, and robust, but fairly coarse, Earth and Sun tracking. Used during initial acquisition and whenever GRACE operates in safe mode.
- Center of Mass Trim Assembly (MTA): Precisely measures the offset between the satellite's center of mass and the "acceleration-proof" mass and adjusts center of mass as needed during the flight.
- BlackJack GPS Receiver and Instrument Processing Unit (GPS): Provides digital signal processing; measures the distance change relative to the GPS satellite constellation.
- Globalstar Silicon Solar Cell Arrays (GSA): Covers the outer shell of the spacecraft and generates power.

It is shown, that GRACE delivers the highest temporal resolution and is thus able to observe monthly mass variation with a spatial resolution of less than 1000 km. In [24] it was predicted that GRACE would be able to measure these effects with an accuracy of about 2 mm of water equivalent heights. Though this accuracy has not yet been achieved because of the errors in spherical harmonic coefficients of short-wavelength, it was shown in many publications that the Stokes coefficients from GRACE indeed contain hydrological signals as the monthly solutions from GRACE showed a good agreement with mass variations from hydrological models.

The GRACE mission ended in the October 2017. GRACE-FO (Figure 1.3), which launched May 22, 2018, continues tracking Earth's water movement to monitor changes in underground water storage, the amount of water in large lakes and rivers, soil moisture, ice sheets and

glaciers, and sea level caused by the addition of water to the ocean. This leads to a data gap in time series.

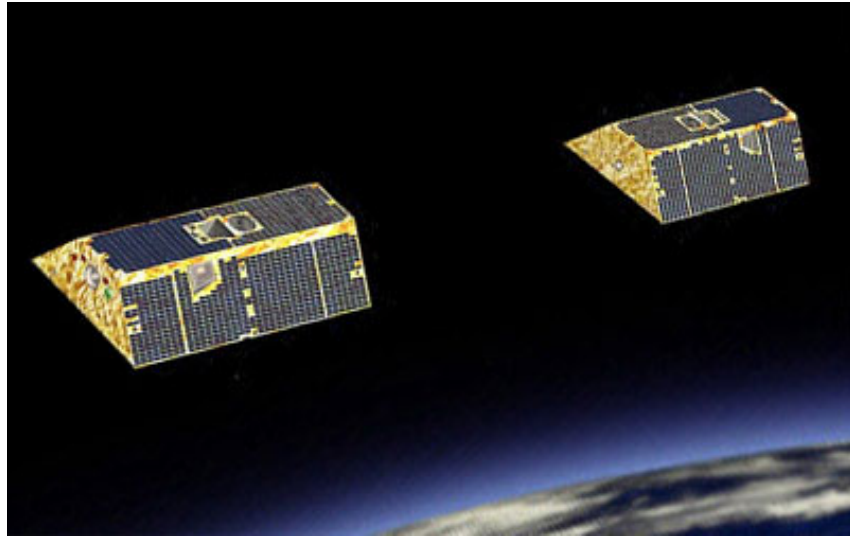


Figure 1.3: GRACE-FO twin satellites https://space.skyrocket.de/doc_sdat/grace-fo.htm

1.3 Motivation

In hydrology, most variables are observed in time series, including Total Water Storage Anomaly (TWSA). In the hydrological cycle, this should reflect seasonal behavior and is in long term relatively stable. However, it was shown that since the launch of GRACE the TWSA of many areas has increased (Figure 1.4). As can be seen, this happened in East central China, Central North America, Central and Western Brazil etc.[19]. Ob river basin in west Siberia is the major river in Russia and one of the greatest rivers of Asia. It was shown that the total water storage has a positive trend since the launch of GRACE Figure 1.5. The motivation for this work is to determine the time and the reason for this positive tendency with various datasets.

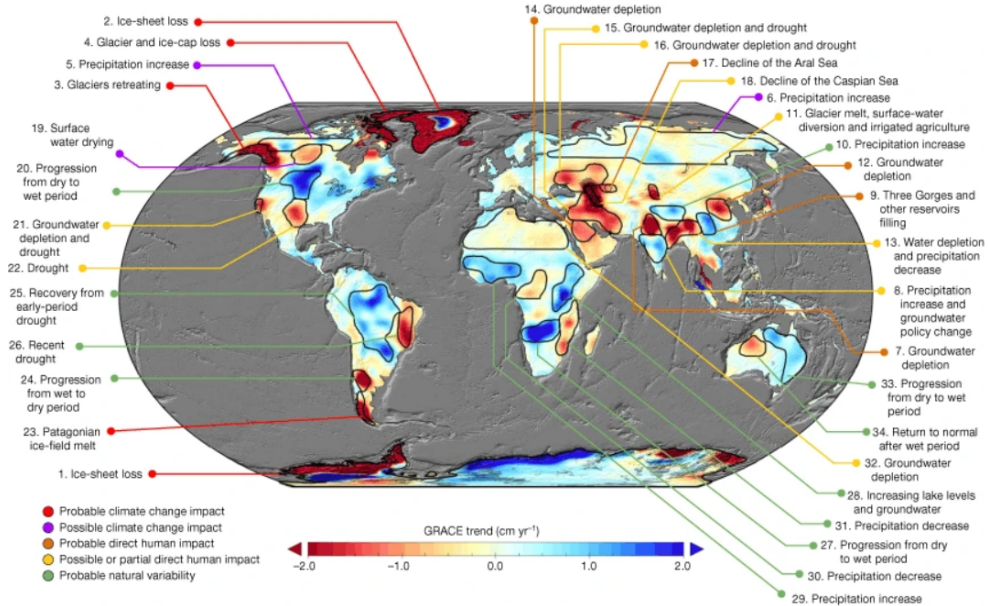


Figure 1.4: Trends in TWS (in centimetres per year) obtained on the basis of GRACE observations from April 2002 to March 2016. The cause of the trend in each outlined study region is briefly explained and colour-coded by category. The trend map was smoothed with a 150 km radius Gaussian filter for the purpose of visualization; however, all calculations were performed at the native 3° resolution of the data product. the figure is adapted from [19]

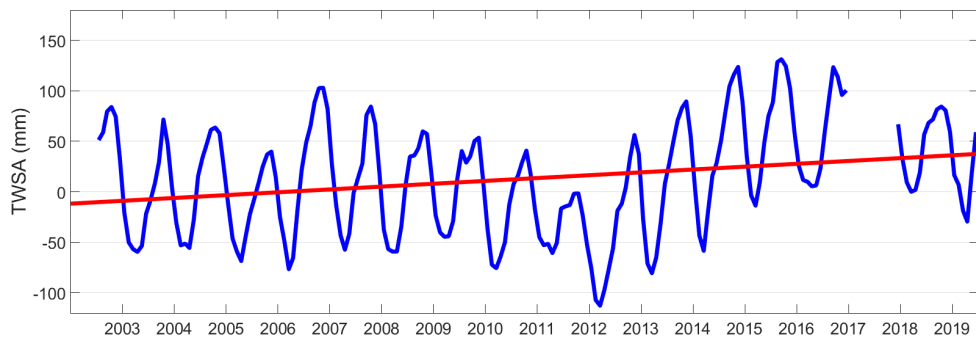


Figure 1.5: Total water storage change from Jan. 2003 to Dec. 2019 in Ob river basin from mascon CSR RL06

Chapter 2

Study Area

Ob River (Figure 2.1), river of central Russia. One of the greatest rivers of Asia, the Ob flows north and west across western Siberia in a twisting diagonal from its sources in the Altai Mountains to its outlet through the Gulf of Ob into the Kara Sea of the Arctic Ocean. It is a major transportation artery, crossing territory at the heart of Russia that is extraordinarily varied in its physical environment and population. Even allowing for the barrenness of much of the region surrounding the lower course of the river and the ice-clogged waters into which it discharges, the Ob drains a region of great economic potential.

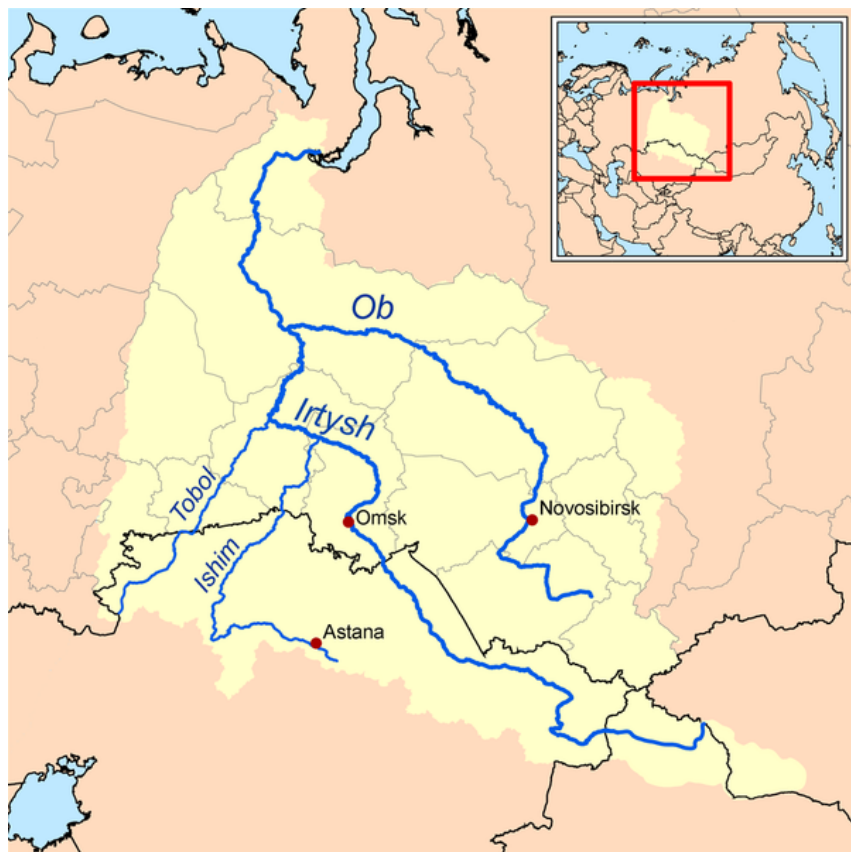


Figure 2.1: River Basins Ob <http://www.geologypage.com/2014/03/ob-river.html>

2.1 Physiography

The Ob proper is formed by the junction of the Biya and Katun rivers, in the foothills of the Siberian sector of the Altai, from which it has a course of 3 650 km. If, however, the Irtysh River is regarded as part of the main course rather than as the Ob's major tributary, the maximum length, from the source of the Black (Chorny) Irtysh in China's sector of the Altai, is 5 410 km, making the Ob the seventh longest river in the world. The catchment area is approximately 2 975 000 square km. Constituting about half of the drainage basin of the Kara Sea, the Ob's catchment area is the sixth largest in the world. The drainage basin is classified as cropland (36%), forest (30%), wetland (11%), grassland (10%), shrub (5%) , developed (5%) and irrigated cropland (3%).[18]

The West Siberian Plain covers about 85 percent of the Ob basin.[13] The rest of the basin comprises the terraced plains of Turgay (Kazakhstan) and the small hills of northernmost Kazakhstan in the south and the Kuznetsk Alatau range, the Salair Ridge, the Altai Mountains and their foothills and outliers in the southeast.

The huge basin of the Ob stretches across a number of natural zones. Semidesert prevails in the far south around Lake Zaysan (recipient of the Black Irtysh and source of the Irtysh proper), bordered on the north by steppe grassland. The central regions of the West Siberian Plain i.e., more than half of the basin-consist of taiga (swampy coniferous forest), with great expanses of marshland. In the north there are vast stretches of tundra (low-lying, cold-tolerant vegetation).

2.2 Climate

According to Koeppen-Gerger climate classification, major part of Ob basin belongs to Subarctic climate(Dfc) 2.2 [17]. It has short, warm summers and long, cold winters. Average January temperatures range from -28°C on the shores of the Kara Sea to -16°C in the upper reaches of the Irtysh. July temperatures for the same locations, respectively, range from 4°C to above 20°C . The absolute maximum temperature, in the arid south, is 40°C ,[13] and the minimum, in the Altai Mountains, is -60° . Rainfall, which occurs mainly in the summer, averages less than 400 mm per year in the north, 500 to 600 mm in the taiga zone, and 300 to 400 mm on the steppes. The western slopes of the Altai receive as much as 1 575 mm per year. Snow cover lasts for 240 to 270 days in the north and for 160 to 170 days in the south. It is deepest in the forest zone, where it ranges from 60 to 90 cm, and in the mountains, where it averages 200 cm per year. It is much shallower on the tundra, ranging from 30 to 50 cm, and very thin on the steppe, where 20 to 40 cm fall.[13]

On the upper Ob the spring floods begin early in April, when the snow on the plains is melting; and they have a second phase, ensuing from the melting of snow on the Altai Mountains. The middle Ob, scarcely affected by the upper Ob's phases, has one continuous spring-summer period of high water, which begins in mid April. For the lower Ob, high water begins in late April or early May. Levels, in fact, begin to rise when the watercourse is still obstructed by ice; and maximum levels, which occur by May on the upper Ob, may not be reached until June, July, or even August on the lower reaches. For the upper Ob, the spring

floods end by July, but autumn rains bring high water again in September and October; in the middle and lower Ob, the spring and summer floodwaters gradually recede until freezing sets in. On the lower reaches, flooding may last four months. Flooding of the Ob proper and of the Irtysh obstructs the minor tributaries' drainage.

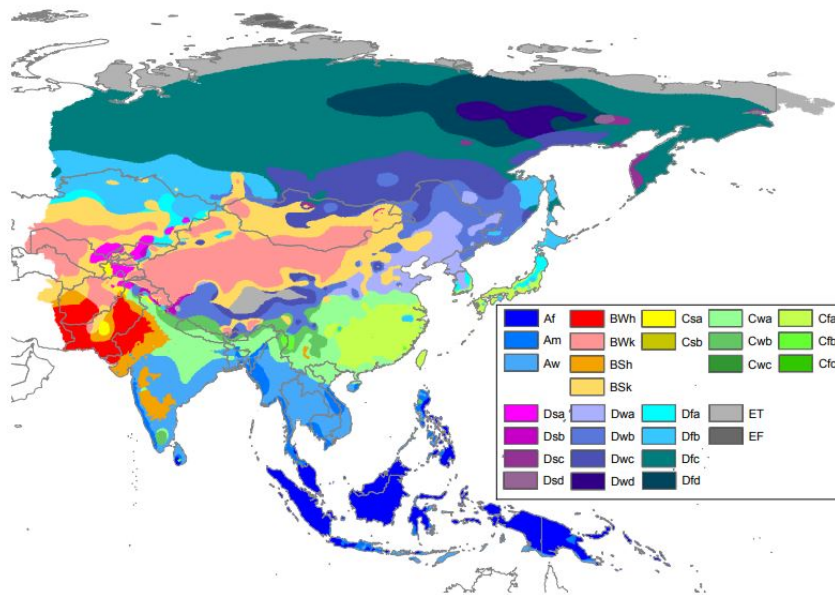


Figure 2.2: Asia Map of Koeppen-Geiger climate classification [17]

2.3 Hydrology

The Ob has the third greatest discharge of Siberia's rivers, after the Yenisey and the Lena. On average, it pours some 400 cubic km of water annually into the Arctic Ocean about 12% of that ocean's total intake from drainage. The volume of flow at Salekhard, just above the delta, is about 42 000 cubic metres per second at its maximum and 2 000 cubic metres per second at its minimum, while for Barnaul, on the upper Ob, the corresponding figures are 9 600 and 200 cubic metres per second. The average annual discharge rate at the river's mouth is about 12 700 cubic metres per second. Most of the water comes from the melting of seasonal snow and from rainfall; much less of it comes from groundwater, mountain snow, and glaciers.[13]

2.4 Permafrost

Permafrost is ground that continuously remains frozen for two or more years, located on land or under the ocean. Permafrost currently underlies significant portions of the six largest Arctic basin [7] which include Ob river Basin. Permafrost is formed from ice holding various types of soil, sand, and rock in combination [4]. In recent years, as Earth's warms, the permafrost is thawing, which means the permafrost melts, leaving behind water and soil [4].

2.5 Human use

Basin total population is about 27 million, with 39 cities having a population of more than 100 000. The Ob's immense hydroelectric potential is estimated at some 250 billion kilowatts. Three main stations have been built: one on the Ob proper, at Novosibirsk, and the other two on the mountainous reaches of the Irtysh, at Bukhtarma and Oeskemen. Both industry and agriculture have been intensively developed in the Ob basin. Cities such as Omsk, Novosibirsk, and Barnaul are major industrial and manufacturing centres. The steppe zone, in the southern Ob basin, is the major producer of spring wheat in Russia. The west Siberian oil and gas fields, located in the taiga and tundra zones of the middle and lower Ob, are the most important in Russia, contributing about two-thirds of the country's crude oil and natural gas output.

Chapter 3

Data

3.1 GRACE and GRACE-FO

3.1.1 Spherical harmonics

The variations in the gravity field impacts on both GRACE satellites at different times, such deviations cause a change in the inter-satellite range, which is measured with very high accuracy from the K-band measurement unit. The measured inter-satellite range can be transformed into changes in the Earth's gravity field, which is described with the Stokes coefficients \tilde{C}_{lm} and \tilde{S}_{lm} .

There is only one Earth gravity field and all centers start off with identical GRACE Level-1 observations, but deriving month-to-month gravity field variations from GRACE observations requires a complex inversion of relative ranging observations between the two formation-flying GRACE spacecraft, in combination with precise orbit determination via GPS and various corrections for spacecraft accelerations not related to gravity changes. Many parameter choices and solution strategies are possible, and have been explored by different data centers. In this thesis the solutions from JPL, CSR, GFZ and ITSG are used, which allows the calculation of gravity field and equivalent water height anomaly. Appendix A shows the method of estimating TWS from GRACE spherical harmonics:

$$h_W(\theta, \lambda; t) = \frac{R\rho_{ave}}{3\rho_W} \sum_{l=0}^{\infty} \frac{2l+1}{1+k_l} \sum_{m=0}^l \tilde{P}_{lm}(\cos \theta) (\Delta\tilde{C} \cos m\lambda + \Delta\tilde{S} \sin m\lambda) \quad (3.1)$$

3.1.2 Mass concentration

Spherical harmonics have been well studied and widely used in satellite geodesy for several decades, based on the computational efficiency of the parameterization, and because the satellite sensitivity is dependent on the spatial wavelength of the mass variations which is implicit in the harmonic basis function. However, unconstrained harmonic solutions from GRACE have typically suffered from poor observability of east-west gradients, resulting in the so-called "stripes" that are conventionally removed via empirical smoothing and/or "destriping" algorithms. Although quite effective, especially for larger spatial scales, the destriping also removes some real geophysical signal along with the stripes, and the size, shape, and orientation of the signals strongly affect the effectiveness of destriping.[25]

Thus, to confirm the reliability of spherical harmonic, another common function would be taken into consideration to estimate mass flux from GRACE, which is called mass concentration(mascon). Each mass tile are defined as a finite truncated spherical harmonic representation up to degree and order 120, which are in turn related to the range-rate observation via their partial derivatives. The size of each tile is approximately 1° equatorial longitudinal distance. The mass anomaly for each of the mass tile is estimated using the KBR range-rate observations and the associated spherical harmonic partial derivatives and the singular estimation process is stabilized using Tikhonov regularization solutions with time-variable regularization matrix. [20].

This mascon solutions have no stripe errors and capture all the signals observed by GRACE within the measurement noise level. The solutions are not tailored for specific applications and are global in nature.[20] In this thesis the mascon solution from CSR are compared with

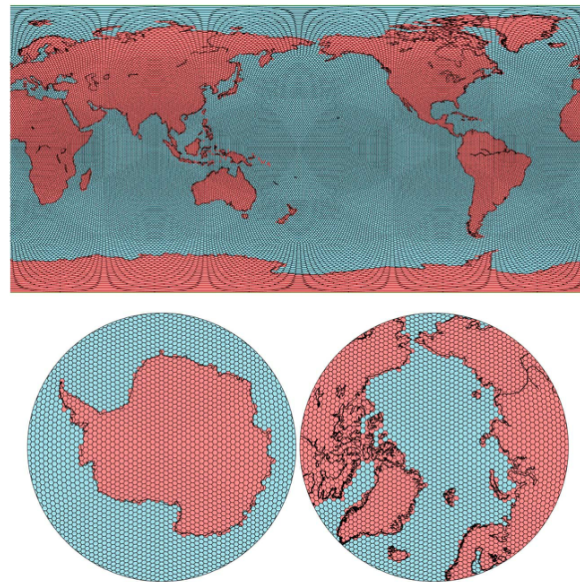


Figure 3.1: The distribution of 40,962 geodesic grid tiles over the Earth used as a basis function for estimation of mass anomalies from GRACE for CSR mascon solutions. (top) Global view, (bottom left) South Pole view, and (bottom right) North Pole view [20]

the results from spherical harmonic solutions.

3.2 Precipitation

Gauge observations are typically used to measure precipitation directly at the Earth's surface [12]. Various large-scale climate data sets at different spatiotemporal scales have been developed from station (in situ) observations. These different types of precipitation data product have proved useful across a wide range of fields of research [21]. In this thesis the precipitation data from 9 data resources are gathered and processed (Table 3.1). The methods dealing with these data sets will be discussed later:

Dataset	Timespan	Temporal Resolution	Spatial Resolution	Spatial Coverage
PREC/L	1948 - present	Monthly	$0.5^\circ \times 0.5^\circ$	Global
CPC	1979 - present	Monthly , Daily	$0.5^\circ \times 0.5^\circ$	Global
GPCP	1979 - present	Monthly	$2.5^\circ \times 2.5^\circ$	Global
CMAP	1979 - present	Monthly	$2.5^\circ \times 2.5^\circ$	Global
PERSIANN-CDR	1983 - present	Monthly , Daily	$0.25^\circ \times 0.25^\circ$	$60S^\circ - 60N^\circ$
NCEP1	1948 - present	Monthly , Daily	$2.5^\circ \times 2.5^\circ$	Global
NCEP2	1979 - present	Monthly , Daily	$1.875^\circ \times 1.875^\circ$	Global
ERA5	1979 - present	Monthly	$31\text{ km} \times 31\text{ km}$	Global
MERRA-2	1980- present	Monthly , Daily	$0.5^\circ \times 0.625^\circ$	Global

Table 3.1: precipitation datasets

Precipitation reconstruction over land (PREC/L) PREC/L if provided from National Oceanic and Atmospheric Administration (NOAA).It is derived from gauge observations from over 17 000 stations collected in the Global Historical Climatology Network(GNCN), and the Climate Anomaly Monitoring System(CAMS) datasets. By using OI analysis procedure, the monthly gridded analyses of precipitation over the global land area since 1948 are presented. The mean distribution and annual cycle of precipitation observed in the PREC/L showed good agreement with those in several published gauge-based datasets. [3]

CPC unified gauge-based analysis of global daily precipitation This dataset is provided from Climate Prediction Center(CPC). A gauge-based analysis of daily precipitation has been constructed over the global land areas. Gauge reports from over 30 000 stations are collected from multiple sources including GTS, COOP, and other national and international agencies. Quality control is performed through comparisons with historical records and independent information from measurements at nearby stations, concurrent radar / satellite observations, as well as numerical model forecasts. Quality controlled station reports are then interpolated to create analyzed fields of daily precipitation with consideration of orographic effects [27]. The daily analysis is constructed on a 0.125 degree lat/lon grid over the entire global land areas, and released on a 0.5 degree lat/lon grid over the global domain for a period from 1979 to the present.[26] This dataset has two components: (a) the "retrospective version" which uses 30K stations and spans 1979-2005 and (b) the "real-time version" which uses 17K stations and spans 2006-present.

Global Precipitation Climatology Project (GPCP) In this dataset, precipitation data from rain gauge stations, satellites and sounding obsevations have been merged to estimate monthly rainfall on a 2.5 degree global grid since 1979. It provides a consistent analysis of global precipitation from the integration of various satellite data sets of lands and oceans and a gauge analysis over land.

CPC Merged Analysis of Precipitation (CMAP) This data set is also constructed from an analysis of gauge data and satellite-derived precipitation estimates. The overlapping satellite and reanalysis-based estimates are weighted according to their fit with the gauge-based analysis. The quality of this is in general the best in the tropics and weakens towards the polar regions.

Precipitation Estimation from Remotely Sensed Information using Artificial Neural Networks - Climate Data Record(PERSIANN-CDR) This data set provides daily rainfall estimates at a spatial resolution of 0.25 degrees in the latitude band 60S - 60N from 1983 to the near-present. The precipitation estimate is produced using the PERSIANN algorithm on GridSat-B1 infrared satellite data, and the training of the artificial neural network is done using the National Centers for Environmental Prediction (NCEP) stage IV hourly precipitation data. The PERSIANN-CDR is adjusted using the Global Precipitation Climatology Project (GPCP) monthly product.

NCEP/NCAR Reanalysis 1&2 The NCEP/NCAR Reanalysis 1 project is using a state-of-the-art analysis/forecast system to perform data assimilation using past data from 1948 to the present. The system has been designed with advanced quality control and monitoring components, and can produce 1 mon of reanalysis per day on a Cray YMP/8 supercomputer. Different types of output archives are being created to satisfy different user needs[11]. The NCEP Reanalysis 2 is the improvement of the NECP Reanalysis 1.

ERA5 ERA5 is produced using 4D-Var data assimilation in CY41R2 of ECMWF's Integrated Forecast System (IFS), with 137 hybrid sigma/pressure (model) levels in the vertical, with the top level at 0.01 hPa. Atmospheric data are available on these levels and they are also interpolated to 37 pressure, 16 potential temperature and 1 potential vorticity level(s). [10]"Surface or single level" data are also available, containing 2D parameters such as precipitation, 2m temperature, top of atmosphere radiation and vertical integrals over the entire atmosphere. The IFS is coupled to a soil model, the parameters of which are also designated as surface parameters, and an ocean wave model.

The ERA5 dataset contains one (hourly, 31 km) high resolution realisation (referred to as "reanalysis" or "HRES") and a reduced resolution ten member ensemble (referred to as "ensemble" or "EDA"). Generally, the data are available at a sub-daily and monthly frequency and consist of analyses and short (18 hour) forecasts, initialised twice daily from analyses at 06 and 18 UTC.[10] Most analysed parameters are also available from the forecasts. There are a number of forecast parameters, e.g. mean rates and accumulations, that are not available from the analyses. The daily total precipitation can then be calculated from ERA5 data using python with the help of CDS API.

Modern-Era Retrospective analysis for research and Applications, version 2 (MERRA-2)

This is a global atmospheric reanalysis produced by the NASA Global Modeling and Assimilation Office(GMAO). It spans the satellite observing era from 1980 to the present. The goals of MERRA-2 are to provide a regularly-gridded, homogeneous record of the global atmosphere, and to incorporate additional aspects of the climate system including trace gas constituents (stratospheric ozone), and improved land surface representation, and cryospheric processes.

3.3 Evapotranspiration

Evaporation is the process whereby liquid water is converted to water vapour (vaporization) and removed from the evaporating surface (vapour removal). Water evaporates from a variety of surfaces, such as lakes, rivers, pavements, soils and wet vegetation. 6 datasets are used in this thesis (Table 3.2).

Dataset	Timespan	Temporal Resolution	Spatial Resolution	Spatial Coverage
GLDAS NOAH	2000 - present	Monthly	$0.25^\circ \times 0.25^\circ$	$60^\circ S - 90^\circ N$
GLDAS CLSM	2000 - present	Monthly	$0.25^\circ \times 0.25^\circ$	$60^\circ S - 90^\circ N$
GLDAS VIC	2000 - present	Monthly	$0.25^\circ \times 0.25^\circ$	$60^\circ S - 90^\circ N$
FLDAS	2002 - present	Monthly	$0.1^\circ \times 0.1^\circ$	$60^\circ S - 90^\circ N$
SSEBop	2003- present	Monthly	$0.0097^\circ \times 0.0097^\circ$	$60^\circ S - 60^\circ N$
ERA5	1979 - present	Monthly	31 km \times 31 km	Global

Table 3.2: evapotranspiration datasets

The Global Land Data Assimilation System (GLDAS) Direct measurements and data acquisition of ET are very difficult and expensive, especially at the global level. Therefore, modeling is one common alternative for estimating ET. GLDAS has been generating quality-controlled, spatially and temporally consistent, terrestrial hydrologic data, including ET and other variants. The goal of GLDAS is to ingest satellite- and ground*based observational data products, using advanced land surface modeling and data assimilation techniques, in order to generate optimal fields of land surface states and fluxes.

The high-quality, global land surface fields provided by GLDAS support several current and proposed weather and climate prediction, water resources applications, and water cycle investigations. The project has resulted in a massive archive of modeled and observed, global, surface meteorological data, parameter maps, and output which includes 1-degree and 0.25-degree resolution 1948-present simulations of the NOAH, Common Land Model (CLM), Variable Infiltration Capacity Model (VIC), Mosaic, and Catchment Land Surface Models (CLSM). NOAH, CLSM and VIC are used in this thesis.

Famine Early Warning Systems Network (FEWS NET) Land Data Assimilation System (FLDAS) The goal of the FLDAS project is to achieve more effective use of limited available hydroclimatic observations and is designed to be adopted for routine use for FEWS NET

decision support. It is a custom instance of the NASA Land Information System (LIS) that has been adapted to work with domains, data streams, and monitoring and forecast requirements associated with food security assessment in data-sparse, developing country settings. Adopting LIS allows FEWS NET to leverage existing land surface models and generate ensembles of soil moisture, ET, and other variables based on multiple meteorological inputs or land surface models.

optiaonal Simplified Surface Energy Balance (SSEBop) The SSEBop seTup is based on the Simplified Surface Energy Balance (SSEB) approach with unique parameteriyation for operational application combines ET fractions generated from remotely sensed MODIS thermal imagery, acquired every 8 days, with reference ET using a thermal index approach. The unique feature of the SSEBop parameterization is that it uses pre-defined, seasonally dynamic, boundary conditions that are unique to each pixel for the hot/dry and cold/wet reference points.

3.4 Runoff

3.4.1 Global datasets

Runoff is quantity of water discharged in surface streams. Runoff includes not only the waters that travel over the land surface and through channels to reach a stream but also interflow, the water that infiltrates the soil surface and travels by means of gravity toward a stream channel (always above the main groundwater level) and eventually empties into the channel. Runoff also includes groundwater that is discharged into a stream; streamflow that is composed entirely of groundwater is termed base flow, or fair-weather runoff, and it occurs where a stream channel intersects the water table.

The in-situ run off data are from Global Runoff Data Center (GRDC). The GRDC is an international archive of data up to 200 years old, and fosters multinational and global long-term hydrological studies. Originally established three decades ago, the aim of the GRDC is to help earth scientists analyse global climate trends and assess environmental impacts and risks. Operating under the auspices of WMO the database of quality controlled "historical" mean daily and monthly discharge data grows steadily and currently comprises river discharge data of more than 9,900 stations from 159 countries.

However, the discharge data from GRDC of Ob river are only up to 2010, which doesn't fit the purpose totally. Thus, like precipitation and evapotranspiration, models from different data centers are considered. Table 3.3. But it is shown later, that these datasets are not good enough. In addition to those hydrological models, the altimetry measurement using satellite is also taken into consideration since the station for in-situ discharge(Salekhard)(Figure 3.2) is known.

3.4.2 Water level height

Among the space-borne sensors, satellite altimetry can provide surface water height successively with repeat periods of 10 and 35 days. Although satellite altimetry was initially

Dataset	Timespan	Temporal Resolution	Spatial Resolution
GLDAS NOAH	2000 - present	Monthly	$0.25^\circ \times 0.25^\circ$
GLDAS CLSM	2000 - present	Monthly	$0.25^\circ \times 0.25^\circ$
GLDAS VIC	2000 - present	Monthly	$0.25^\circ \times 0.25^\circ$
ERA5	1979 - present	Monthly	$31\text{ km} \times 31\text{ km}$
HTESEL	1979 - 2012	Monthly	$0.25^\circ \times 0.25^\circ$
LISFLOOD	1980 - 2011	Monthly	$0.25^\circ \times 0.25^\circ$
ORCHIDEE	1980 - 2014	Monthly	$0.25^\circ \times 0.25^\circ$
PCR-GLOBWB	1979 - 2012	Monthly	$0.5^\circ \times 0.5^\circ$
SURFEX	1980 - 2014	Monthly	$0.25^\circ \times 0.25^\circ$
W3RA	1979 - 2012	Monthly	$0.5^\circ \times 0.5^\circ$
WaterGAP3	1980 - 2014	Monthly	$0.25^\circ \times 0.25^\circ$

Table 3.3: runoff datasets



Figure 3.2: Station Salekhard

designed for oceanography, four decades of altimetry missions have provided an opportunity to study the continental hydrological cycle as well. By using the methods mentioned later, the runoff can be estimated from the satellite water level.

Altimetry satellites basically determine the distance from the satellite to a target surface by measuring the satellite-to-surface round-trip time of a radar pulse. However, this is not the only measurement made in the process, and a lot of other information can be extracted from altimetry.

The magnitude and shape of the echoes (or waveforms) also contain information about the characteristics of the surface which caused the reflection. The best results are obtained over the ocean, which is spatially homogeneous, and has a surface which conforms with known statistics.

Envisat Envisat (Environmental Satellite) is a large inactive Earth-observing satellite which is still in orbit. Operated by the European Space Agency (ESA), it was the world's largest civilian Earth observation satellite. It was launched on 1 March 2002 aboard an Ariane 5 from the Guyana Space Centre in Kourou, French Guiana, into a Sun synchronous polar orbit at an altitude of 790 ± 10 km. It orbits the Earth in about 101 minutes, with a repeat cycle of 35 days. After losing contact with the satellite on 8 April 2012, ESA formally announced the end of Envisat's mission on 9 May 2012.

In working towards the global and regional objectives of the mission, numerous scientific disciplines currently use the data acquired from the different sensors on the satellite to study such things as atmospheric chemistry, ozone depletion, biological oceanography, ocean temperature and colour, wind waves, hydrology (humidity, floods), agriculture and arboriculture, natural hazards, digital elevation modelling (using interferometry), monitoring of maritime traffic, atmospheric dispersion modelling (pollution), cartography and study of snow and ice.

SARAL SARAL (Satellite with ARgos and ALtiKa) is a cooperative altimetry technology mission of Indian Space Research Organisation (ISRO) and CNES (Space Agency of France). SARAL performs altimetric measurements designed to study ocean circulation and sea surface elevation. The payloads of SARAL are The ISRO built satellite with payloads modules (ALTICKA altimeter), DORIS, Laser Retro-reflector Array (LRA) and ARGOS-3 (Advanced Research and Global Observation Satellite) data collection system provided by CNES was launched by Indian Polar Satellite Launch Vehicle rocket into the Sun-synchronous orbit (SSO). SARAL was successfully launched on 25 February 2013. It will fill the gap between Envisat and the Sentinel 3 mission of the European GMES program.

Sentinel-3 Sentinel-3 is an Earth observation satellite constellation developed by the European Space Agency as part of the Copernicus Programme. The Sentinel-3 mission's main objective is to measure sea-surface topography, sea- and land-surface temperature and ocean- and land-surface colour with accuracy in support of ocean forecasting systems, and for environmental and climate monitoring. Sentinel-3 builds directly on the heritage pioneered by

ERS-2 and Envisat satellites. Near-real time data will be provided for ocean forecasting, sea-ice charting, and maritime safety services on the state of the ocean surface, including surface temperature, marine ecosystems, water quality and pollution monitoring. The satellite orbit provides a 27-day repeat for the topography package, with a 4-day sub-cycle.

Chapter 4

Method

4.1 Estimating hydrological component from datasets

As mentioned before, the terrestrial water balance can be written as:

$$P - ET - R = \frac{dS}{dt} \quad (4.1)$$

where

P	Precipitation
ET	evapotranspiration
R	Surface Runoff
dS/dt	total water storage change

For each, time series from different resources are processed using different methods

Jet Propulsion Laboratory (JPL), Center for Space Research (CSR), German Research Centre for Geosciences (GFZ) and Institute of Theoretical Geodesy and Satellite Geodesy (ITSG) post process Level-1 data of GRACE and provide solutions in terms of spherical harmonics. It should be noted that there is a one-year gap between the GRACE and GRACE-FO and several monthly gaps. This one-year gap would be ignored since we are interested in the long term trend and these monthly gaps are dealt using interpolation. For the equivalent water height we use spline interpolation while for uncertainty we use linear interpolation.

If two known points are given by the coordinates (x_0, y_0) and (x_1, y_1) , the linear interpolant is the straight line between these points. For a value x in the interval (x_0, x_1) , the value y along the straight line is given from the equation of slopes.

$$y = y_0 + (x - x_0) \frac{y_1 - y_0}{x_1 - x_0} \quad (4.2)$$

Spline was a term of elastic rulers that were bent to pass through a number of predefined points (knots). The approach to mathematically modelling the shape of such elastic rulers fixed by $n + 1$ knots is to interpolate between all the pairs of knots and new point with polynomials. In MatLab, both of these interpolation methods can be finished using function *griddedInterpolant*.

We have 4 TWSA time series from CSR, GFZ, ITSG and JPL with different uncertainties. To generate one time series of TWSA for further analyse we use Gaus-Markov model.

4.1.1 Adjustment using Gauss-Markov model

Gauss-Markov model is known as the adjustment with observation equations. The model is as follows

$$\mathbf{y} = \mathbf{Ax} + \mathbf{e} \quad (4.3)$$

where \mathbf{y} is a vector of observations, \mathbf{A} is the design matrix, \mathbf{x} is a vector of unknowns and \mathbf{e} is a vector of measurement errors. Define the *Lagrangian* or *cost function*;

$$\mathcal{L}_a(\mathbf{x}) = \frac{1}{2} \mathbf{e}^T \mathbf{e} \quad (4.4)$$

Then, the adjusted observations can be estimated by using least square criterion, the best \mathbf{x} can be found with the minimum cost function. The equations can be solved as following:

$$\hat{\mathbf{x}} = (\mathbf{A}^T \mathbf{A})^{-1} \mathbf{A}^T \mathbf{y} \quad (4.5)$$

$$\hat{\mathbf{y}} = \mathbf{Ax} = \mathbf{A}(\mathbf{A}^T \mathbf{A})^{-1} \mathbf{A}^T \mathbf{y} \quad (4.6)$$

$$\hat{\mathbf{e}} = \mathbf{y} - \hat{\mathbf{y}} = [\mathbf{I} - \mathbf{A}(\mathbf{A}^T \mathbf{A})^{-1} \mathbf{A}^T] \mathbf{y} \quad (4.7)$$

In many cases, the observations are not equal weighted, which means they have different quality. To solve this problem, we use a matrix \mathbf{P} to describe the weight. The cost function is formed as:

$$\mathcal{L}_a(\mathbf{x}) = \frac{1}{2} \mathbf{e}^T \mathbf{Pe} \quad (4.8)$$

the weighted least squares estimations are:

$$\hat{\mathbf{x}} = (\mathbf{A}^T \mathbf{PA})^{-1} \mathbf{A}^T \mathbf{Py} \quad (4.9)$$

$$\hat{\mathbf{y}} = \mathbf{Ax} = \mathbf{A}(\mathbf{A}^T \mathbf{PA})^{-1} \mathbf{A}^T \mathbf{Py} \quad (4.10)$$

$$\hat{\mathbf{e}} = \mathbf{y} - \hat{\mathbf{y}} = [\mathbf{I} - \mathbf{A}(\mathbf{A}^T \mathbf{PA})^{-1} \mathbf{A}^T \mathbf{P}] \mathbf{y} \quad (4.11)$$

For each month, there are 4 EWH values $S_{CSR}(t), S_{GFZ}(t), S_{ITSG}(t), S_{JPL}(t)$ along with their uncertainty $\sigma_{CSR}(t), \sigma_{GFZ}(t), \sigma_{ITSG}(t), \sigma_{JPL}(t)$. We use the uncertainty to build the weight matrix \mathbf{P} , then we have:

$$\mathbf{y} = \begin{pmatrix} S_{CSR}(t) \\ S_{GFZ}(t) \\ S_{ITSG}(t) \\ S_{JPL}(t) \end{pmatrix} \quad (4.12)$$

$$\mathbf{P} = \begin{pmatrix} \frac{1}{\sigma_{CSR}^2(t)} & 0 & 0 & 0 \\ 0 & \frac{1}{\sigma_{GFZ}^2(t)} & 0 & 0 \\ 0 & 0 & \frac{1}{\sigma_{ITSG}^2(t)} & 0 \\ 0 & 0 & 0 & \frac{1}{\sigma_{JPL}^2(t)} \end{pmatrix} \quad (4.13)$$

$$\mathbf{A} = \begin{pmatrix} 1 \\ 1 \\ 1 \\ 1 \end{pmatrix} \quad (4.14)$$

By inserting Equation 4.12, Equation 4.13 and Equation 4.14 into Equation 4.9 we are able to get one TWSA for one month

$$\hat{\mathbf{x}}_{1 \times 1} = (\mathbf{A}_{1 \times 4}^T \mathbf{P}_{4 \times 4} \mathbf{A}_{4 \times 1})^{-1} \mathbf{A}_{1 \times 4}^T \mathbf{P}_{4 \times 4} \mathbf{y}_{4 \times 1} \quad (4.15)$$

where $\hat{\mathbf{x}}$ is the EWH for one month. By repeating Equation 4.15, we are able to get one whole time series for equivalent water height. The uncertainty for this new time series would be calculated using least squares error:

$$\sigma(t) = \frac{1}{4} \sqrt{\sigma_{CSR}^2(t) + \sigma_{GFZ}^2(t) + \sigma_{ITSG}^2(t) + \sigma_{JPL}^2(t)} \quad (4.16)$$

The derivation of the TWSA would be calculated using central difference:

$$\frac{dS(t)}{dt} = \frac{(dS(t + \Delta t) - dS(t)) + (dS(t) - dS(t - \Delta t))}{2\Delta t} \quad (4.17)$$

$$= \frac{dS(t + \Delta t) - dS(t - \Delta t)}{2\Delta t} \quad (4.18)$$

where Δt is one month. The method used in subsection 4.1.1 also works for precipitation, evapotranspiration and runoff. However, the uncertainties of these time series were unknown. Therefor, it's necessary to get the uncertainty before the adjustment.

We assume that the precipitation and evapotranspiration are normal distributed during 2002 to 2020 (though it is not the case). Under this assumption, the precipitation and evapotranspiration in the same month every year can be regarded as a constant with random errors. We then can use the standard deviation as the uncertainty.

$$\sigma_{Pre_{Jan}} = \sqrt{\frac{\sum_{i=1}^n (Pre(i)_{Jan} - \bar{Pre}_{Jan})^2}{n - 1}} \quad (4.19)$$

where $\sigma_{Pre_{Jan}}$ is the standard deviation of the Precipitation in January, $Pre(i)_{Jan}$ is the precipitation in January in different years and \bar{Pre}_{Jan} is the mean of all the precipitation in January. With the same method we are able to obtain the uncertainty for precipitation and evapotranspiration in other eleven months.

The changing points can be found using moving average (MA). In statistics, a moving average is a calculation used to analyze data points by creating a series of averages of different subsets of the full data set. The reason for calculating the moving average is to help smooth out the data by creating a constantly updated average data. In MatLab, this could be done with *movmean* function. The size of subsets is 12 in this thesis because of the number of months in one year.

After moving average time series the abrupt changes in the mean of the this new series, the sudden change of the time series can be found. This can be achieved using MatLab function *ischange*, which enables user to find the abrupt changes of the a vector in mean value, variance or slope and intercept.

4.2 Estimating the quality of runoff datasets

It was mentioned in section 3.4 that the in-situ runoff data existed til 2010, which allows us to estimate the quality of the data models. First, we calculate the difference between the model and the in-situ data.

$$d(t) = R(t)_{insitu} - R(t)_{model} \quad (4.20)$$

By plotting the cumulative distribution function (CDF) of d , the quality of the model can be estimated. By setting the appropriate quantile we are able to decide if a data model is good enough for further analyze. In this work 10% of the mean in-situ data are set.

4.3 Estimating the runoff using quantile function and water level

The river discharge at the selected gauges is typically determined from an empirical functional relation between water level estimated by satellite altimetry and measured discharges. This relation, referred to as a rating curve, is specific to each gauging station and location of altimetry. However, this technique has many limitations. First, first, this technique is limited by the availability of in situ discharge measurements simultaneous with altimetry data. Second, the location of the altimetry foot- print can also limit the usage of the technique.

Fortunately, [23] provides a methods, which can represent a direct connection between the quantile functions at the corresponding probability and the relationship between runoff and water level.

first, we get the quantile functions for altimetric water level, $Q_R(p)$ and discharge from in situ measurement, $Q_W(p)$:

$$\begin{aligned} Q_R(p) &= \inf(X_R \in R : p \leq F(X_R)) \\ Q_W(p) &= \inf(X_W \in R : p \leq F(X_W)) \end{aligned}$$

where X_R and X_W refer to the runoff and water level values and F represents the CDF. The quantile function specifies, for a given probability $0 < p < 1$, the maximum value that X_R or X_W can attain with that probability.

By achieving the function T between the quantile functions, we can get the function between the runoff and water level since T is a non decreasing function.

$$Q_R = T(Q_W) \implies X_R = T(X_W) \quad (4.21)$$

In principle, the obtained relationship can be used as look-up table implying the desired rating curve. However, as this study aims to compare the statistical and empirical rating curves, a similar way of approximation for both is needed. In this thesis, the simple quadratic estimation is used for modeling the rating curve. Thus, the statistical rating curve is achieved by fitting a quadratic curve over the obtained statistical relationship. Figure 4.1 showed an example of achieving the runoff using water level data from Envisat.

By repeating this process to SARAL and Sentinel missions we can generate an whole runoff time series from 2002 to 2020. (note there is a 32 months gap between Envisat and SARAL from November of 2010 to July of 2013)

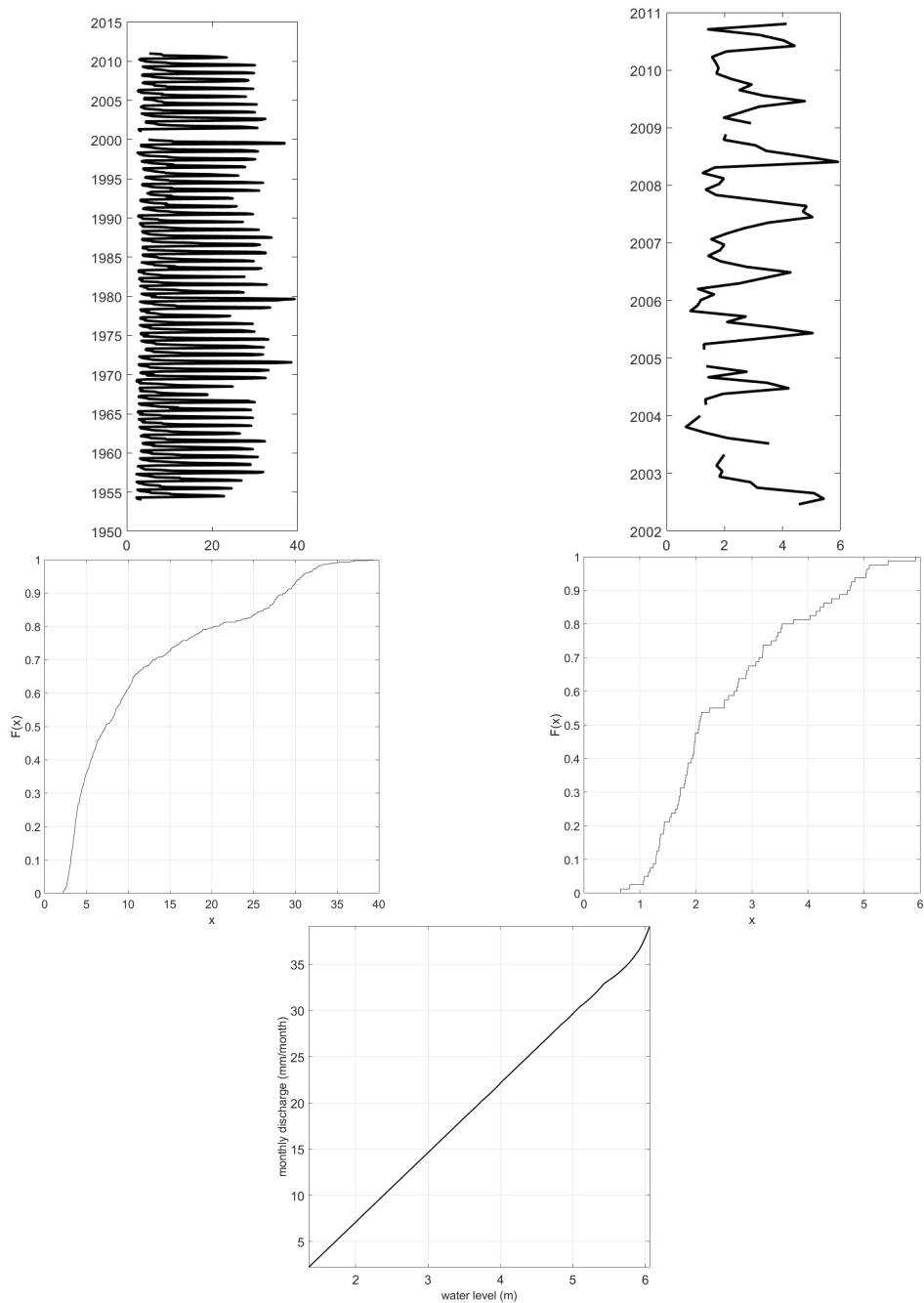


Figure 4.1: Available in-situ runoff for Ob river (top left), estimated water level from Envisat (top right), and quantile function of water level and runoff (middle). A smoothed rating curve is obtained from the corresponding probabilities (bottom)

Chapter 5

Result

5.1 Total water storage

As mentioned in chapter 3, 4 time series (CSR, GFZ, ITSG, JPL) of TWSA from Apr. 2002 to May. 2020 are handled in this work. By using the method in subsection 4.1.1, these four time series can be summarized into one time series Figure 5.1. It is shown that the TWSA increases in summer and decreases in winter annually. As can be seen in this figure, the TWS remains relative stable. We can also see a positive trend from 2013 to 2017 and a negative trend from 2010 to 2012 and after 2017.

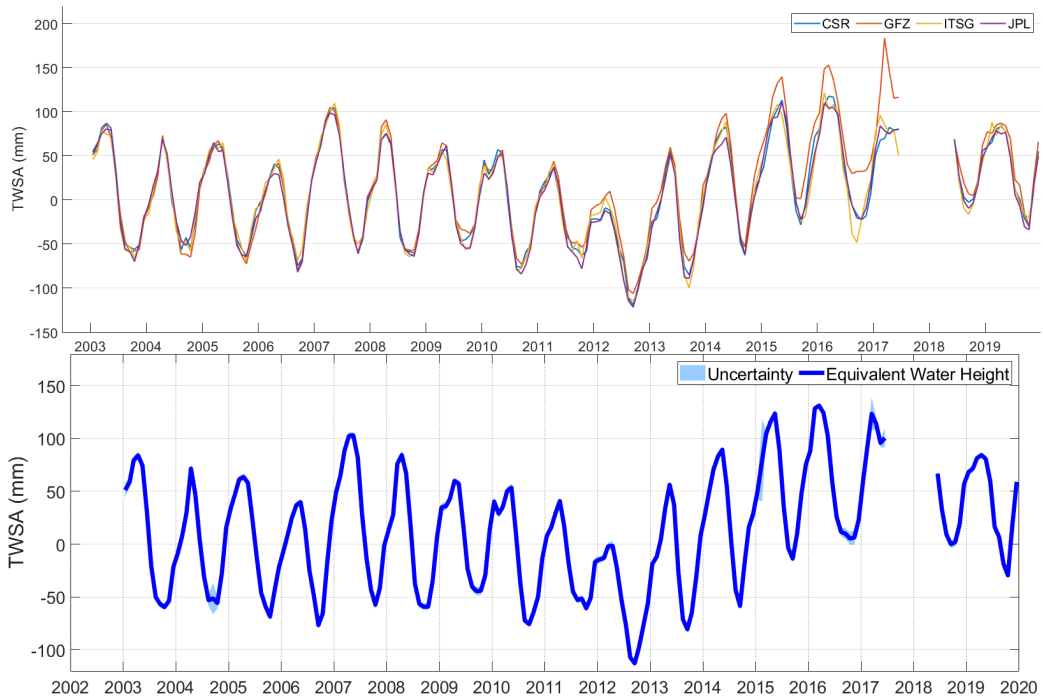


Figure 5.1: TWSA generated from different data centers (top) generate one summarized TWSA time series (bottom) from Jan.2003 to Dec.2019

By using the methods in Equation 4.17 and subsection 4.1.1 2 abrupt change in the deviation of TWSA are found. The time of these two points are October of 2012 and November of 2015, which proves the assumption of positive trend above, while the negative trend between 2010 and 2012 can not be determined. With these 2 points the whole time series can be divided into 3 periods.

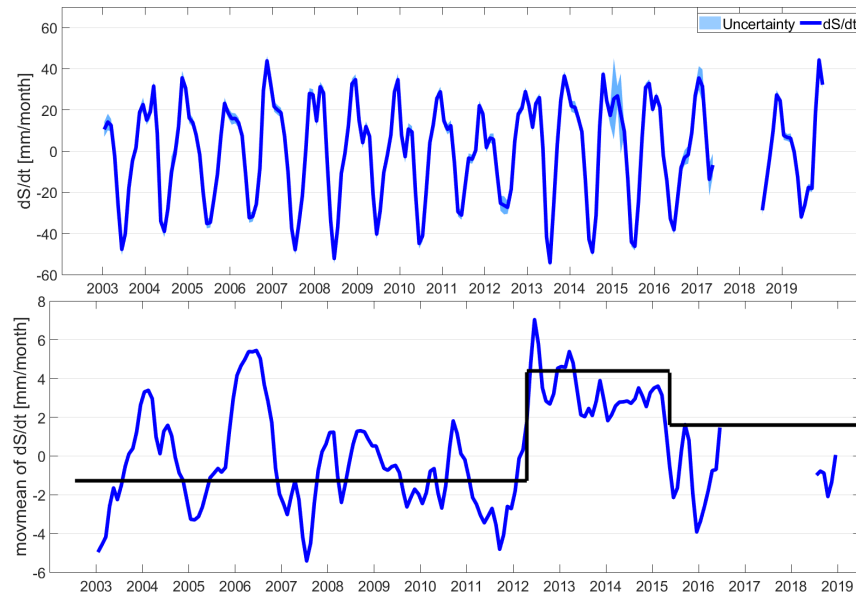


Figure 5.2: the derivation of TWSA (top) and the abrupt change in the moving average (bottom)

After that, the mean dS/dt along with uncertainty in these 3 periods can be calculated Figure 5.3, it is shown that in the first and the third period dS/dt are negative, while in the second period the value is positive. This indicates, that the TWS in the first and the third period were decreasing while the basin has gained water from outside in the second period.

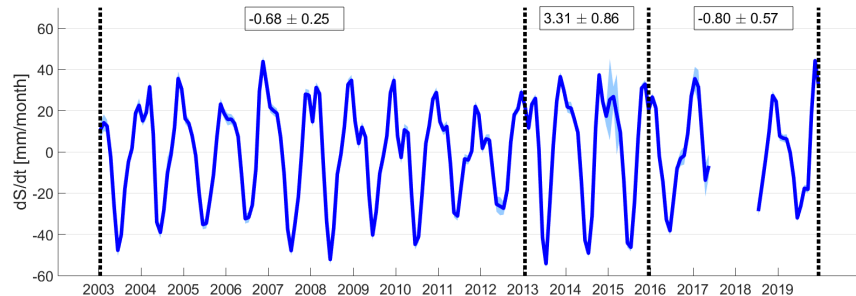


Figure 5.3: mean value with uncertainty of dS/dt and RMSE in 3 periods

As mentioned in chapter 2, the Ob river basin contains a big area. Therefore, it's necessary to confirm, that the behavior of total water storage change is similar among the basin. Figure 5.4 provides mean TWS trend in three periods in Ob basin in gridded area. In the first period, the total water storage remained unchanged in east part but had an slight reduce in west. In the second period, the wast north of the basin obtained a large amount water from outside, but in south east not that much. In the third period, the north west and south east suffered water lost.

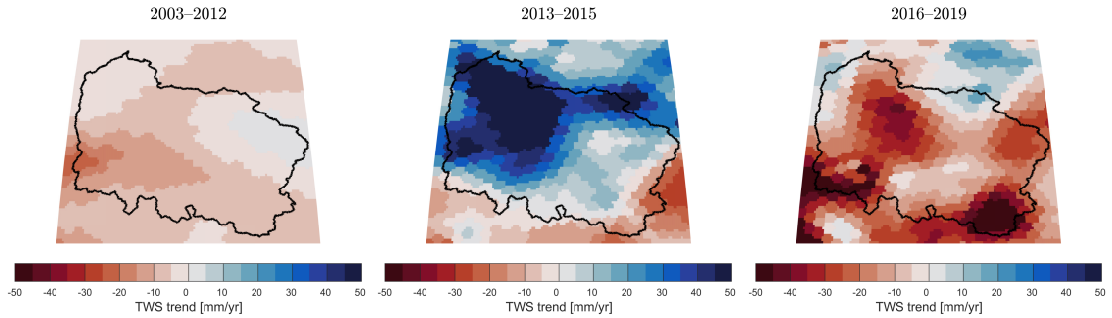


Figure 5.4: spatial TWS change of Ob river basin in each period using mascon CSR RL06 solution

5.2 Precipitation

It was mentioned in chapter 3 that precipitation data from 9 datasets are processed and one time series with uncertainty can be generated by summarizing them Figure 5.5 just as before. The uncertainty are calculated using methods mentioned in subsection 4.1.1.

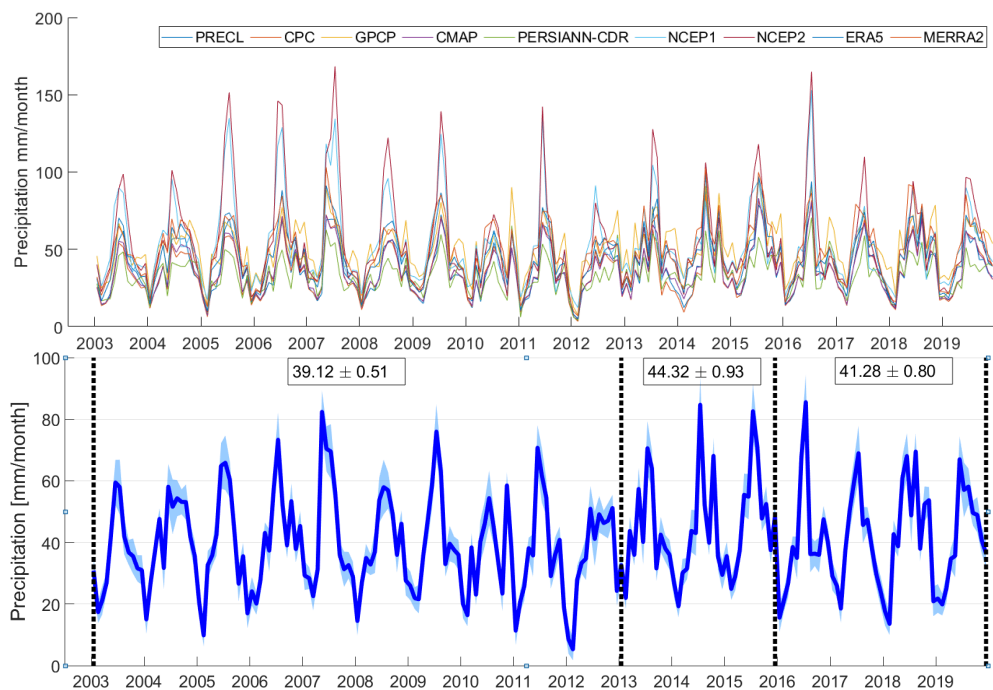


Figure 5.5: all precipitation datasets (top) are summarized into one time series, the mean precipitation with RMSE in 3 periods are calculated (bottom)

By using the same methods for dS/dt , the precipitation are considered into 3 periods, the mean value and uncertainties show that in the second periods the amount of precipitation in this area is 5.2 mm/month bigger than the first period. The precipitation in the third period, however, is less than the second period but still more than the first period.

The spatial information of precipitation from different datasets is also presented Figure 5.6.

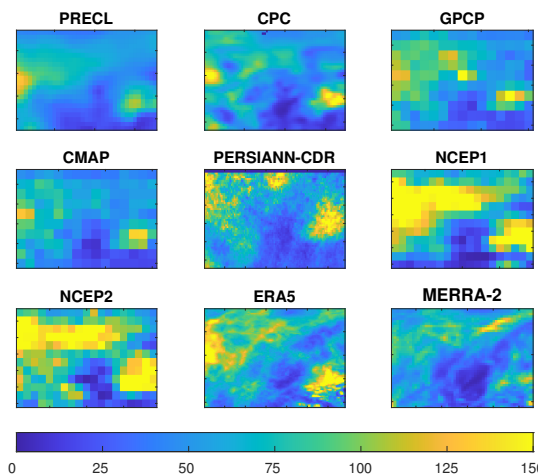


Figure 5.6: spatial change of precipitation in Ob river basin using different datasets in June of 2003

The data in June of 2003 are taken since the precipitation reaches the summit normally in summer. AS we can see, in spite of the different spatial resolution of different datasets it can be detected that the major part of the precipitation took place in west north and east north.

5.3 Evapotranspiration

Like precipitation, the summarized evapotranspiration is presented temporally and the time series is split into 3 periods. The mean value along with uncertainty are also calculated. From Figure 5.7 we can see that the evapotranspiration reaches the summit in summer but nearly disappear in the winter. The results of evapotranspiration is similar to what we see in precipitation: it increases in the second period by 1.54 mm/month and decreases after Dec. 2015 and it didn't go back to the original level in the first period like precipitation. It should also be noted that evapotranspiration has not increased that much in the second period as in precipitation, which follows the rules of water cycle.

The spatial information of evapotranspiration is concluded in Figure 5.8. Same as precipitation, the data from June of 2003 are used for this figure. By comparing different datasets we can find that the evapotranspiration occurs stronger in the east part of the basin.

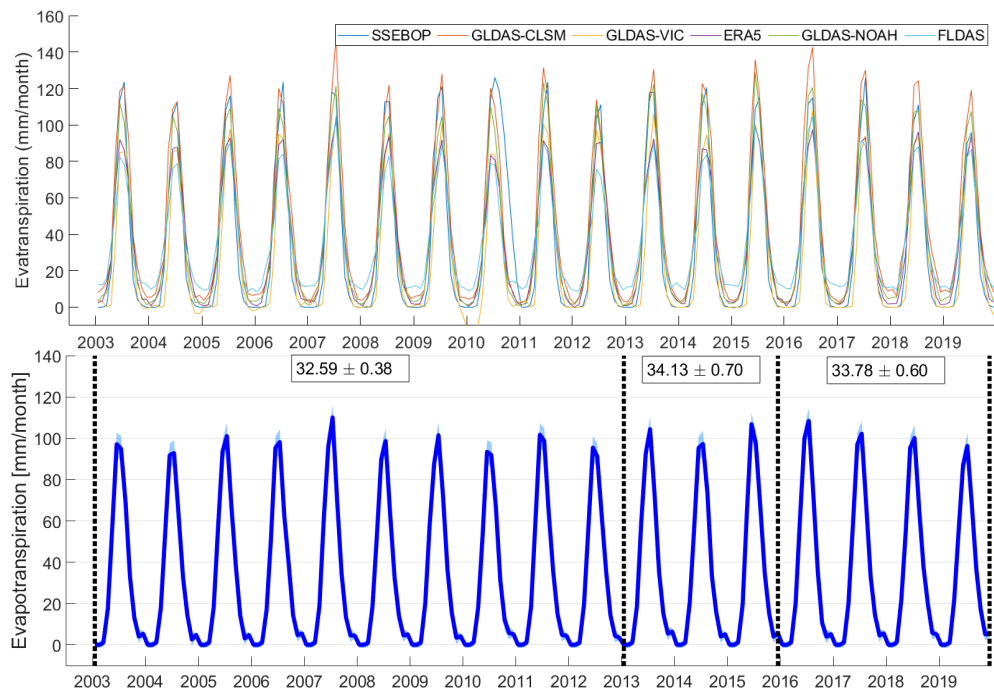


Figure 5.7: all evapotranspiration datasets (top) are summarized into one time series, the mean precipitation with uncertainty in 3 periods are calculated (bottom)

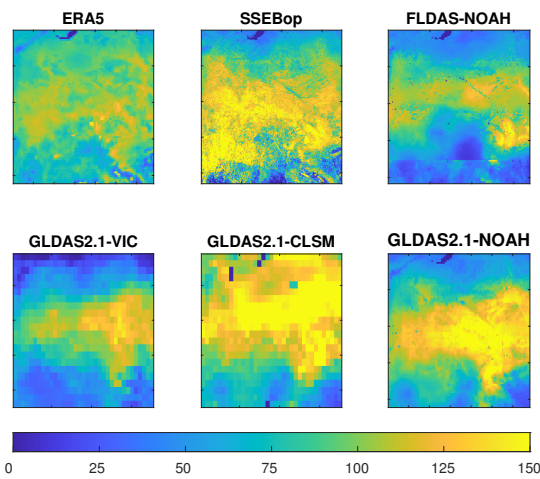


Figure 5.8: spatial change of evapotranspiration in Ob river basin using different datasets in June of 2003

5.4 Runoff

5.4.1 Runoff from global datasets

Like precipitation and evapotranspiration, Runoff data estimated from several models are provided and meanwhile the in-situ data till end of 2010 is available Figure 5.9. It can be seen that the differences between models and in-situ data are not small. By calculating RMSE for these models the quality of them can be estimated. Table 5.1 provides the RMSE for all these datasets, the smallest RMSE is already bigger than 8 mm/month, which is hardly to trust for further analyze.

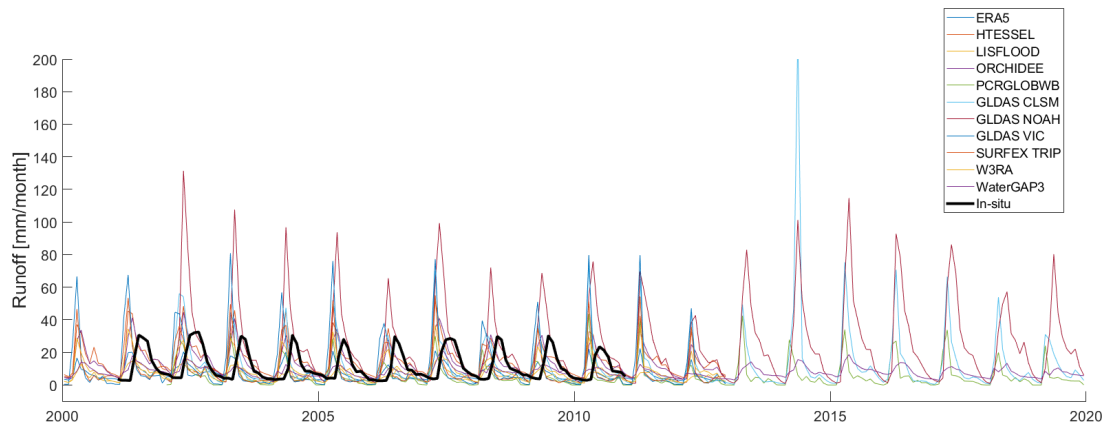


Figure 5.9: Runoff datasets, the black bold time series is the in-situ runoff

Datacenter	RMSE (mm/month)
ERA5	8.18
HTESSEL	10.40
LISFLOOD	11.92
ORCHIDEE	10.24
PCRGLOBWB	9.48
GLDAS CLSM	13.68
GLDAS NOAH	17.01
GLDAS VIC	25.95
SURFEX-TRIP	22.05
W3RA	16.47
WaterGAP3	11.03

Table 5.1: RMSE for runoff datacenters

Then, if we take the CDF of the difference from those models and in-situ data and set 10% of mean in-situ runoff as quantile Figure 5.10 , it is shown that none of these datasets has achieved the standard (90%). Therefor, the runoff would be estimated using satellite altimetry.

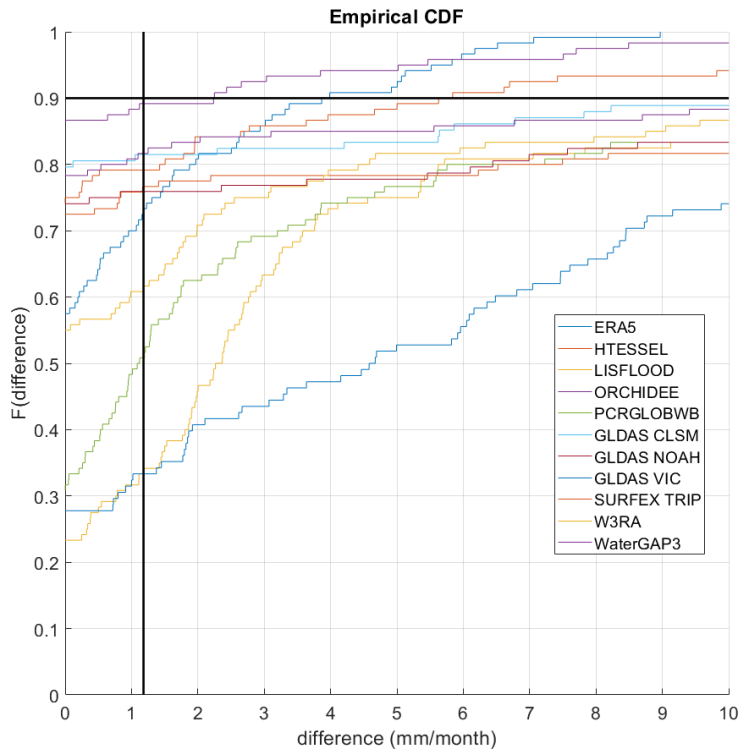


Figure 5.10: CDF of differences

5.4.2 Estimating runoff using quantile function and satellite altimetry

The methods for runoff estimating is introduced in section 3.4, Figure 5.11 presents water level time series from Envisat, SARAL and Sentinel. For each mission 2 virtual stations are chosen. In order to get an accurate runoff, water lever from virtual station closer to Salekhard station are used to generated the final runoff. After combining all 3 time series from different space mission, an runoff time series from Jan. 2001 to Dec. 2019 is obtained Figure 5.12 (top, blue line). Noted that except the gap between Envisat and SARAL, other monthly gaps exists too, these gaps are filled with interpolation Figure 5.12 (top, red line).

Then, as the precipitatin and evapotranspiration, the runoff time series is also divided into 3 periods Figure 5.12 (bottom) and RMSE is calculated from the method section 4.3. It shows that the runoff in the first periods and in the second periods changes not much, but in the third periods the runoff has increased by about 2 mm/month. However, it was found that the runoff are extremely high in 2 months in summer of 2016, since this unusual peak are not found in the water level time series, these 2 months would be ignored. 5.13

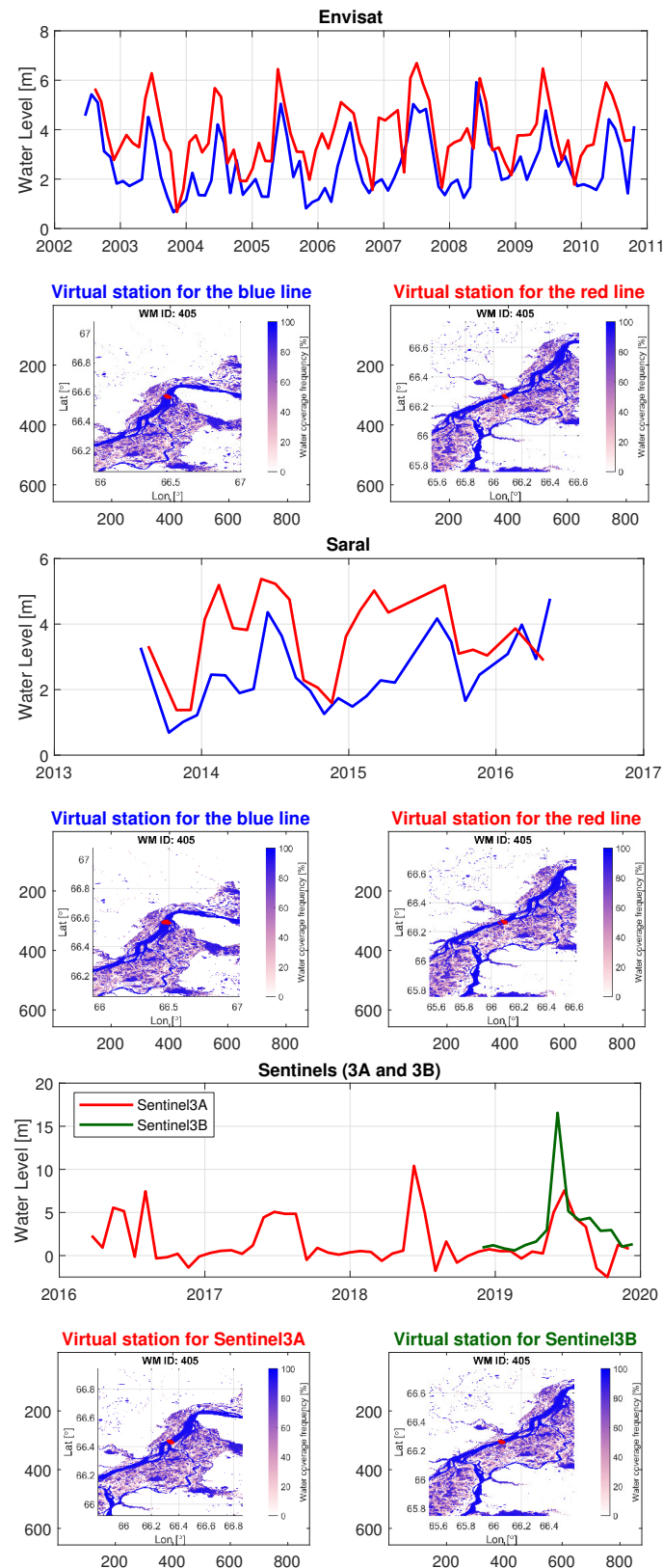


Figure 5.11: water level time series and the location of virtual station for different space mission

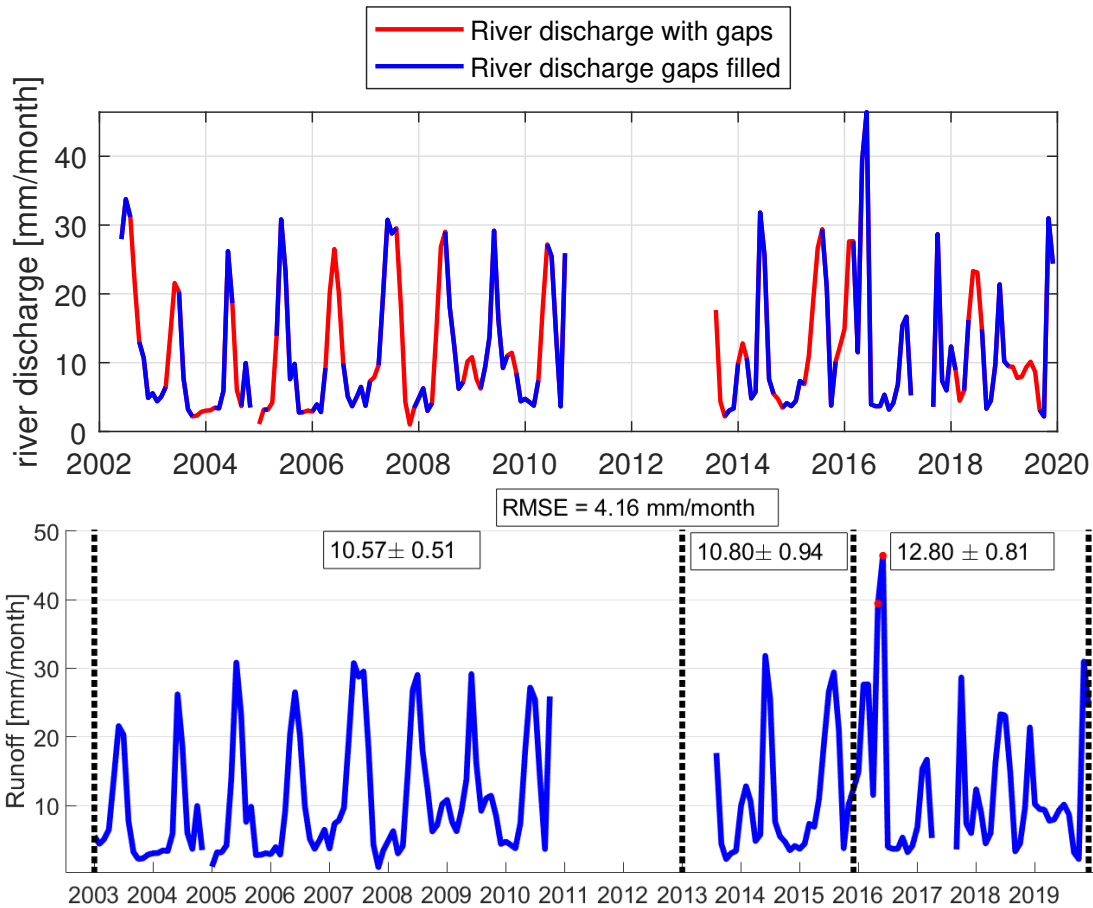


Figure 5.12: runoff timeseries calculated from water level (top) and the mean value in 3 periods, the red points are unusually high and to be ignored(bottom)

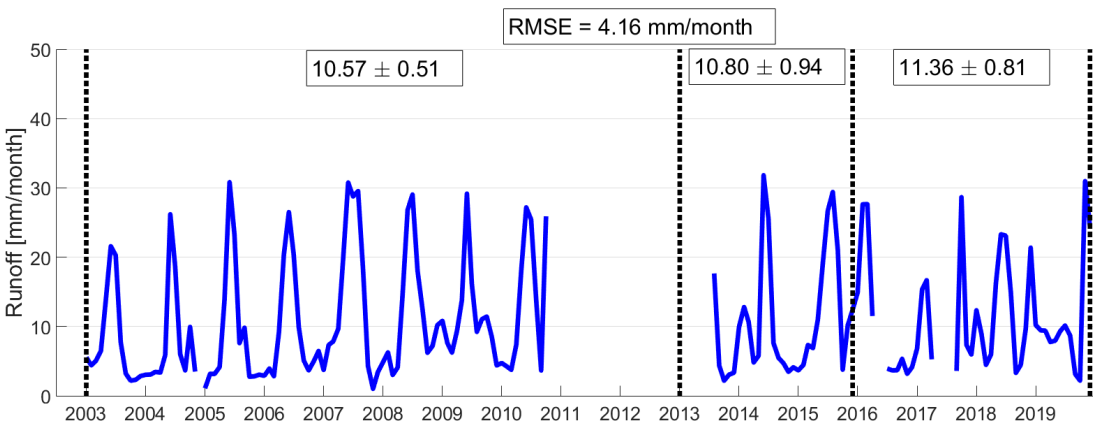


Figure 5.13: runoff time series and mean value in 3 periods after 2 unusual months are ignored

5.5 Discussion about the quality

In order to eliminate the bias between different component, we take the first period as the baseline. Relative dS/dt , precipitation, evapotranspiration and runoff numbers of other 2 period are obtained related to that.

In any case, the equation of terrestrial water balance Equation 1.1 has to be a true statement, which means the result of $P - dS/dt - ET - R$ with uncertainties should be 0. Substituting the results of both periods into this formula can get -0.57 ± 1.63 mm/month for the second period, and 0.29 ± 1.37 mm/month for the third period, which can be acceptable.

Period	2003 to 2012	2013 to 2015	2016 to 2019
dS/dt (mm/month)	-0.68 ± 0.25	3.31 ± 0.86	-0.80 ± 0.57
P (mm/month)	39.12 ± 0.35	44.32 ± 0.64	41.28 ± 0.55
ET (mm/month)	32.59 ± 0.21	34.13 ± 0.38	33.78 ± 0.33
R (mm/month)	10.57 ± 0.51	10.80 ± 0.94	11.36 ± 0.81
Related to the first period			
dS/dt (mm/month)	-	4.00 ± 0.89	-0.11 ± 0.62
P (mm/month)	-	5.20 ± 0.72	2.15 ± 0.65
ET (mm/month)	-	1.53 ± 0.43	1.19 ± 0.38
R (mm/month)	-	0.23 ± 1.07	0.79 ± 0.96
$P - dS/dt - ET - R$ (mm/month)	-	-0.57 ± 1.63	0.29 ± 1.37

Table 5.2: mean value of all water cycle component in 3 periods with uncertainties

Chapter 6

Conclusion and outlook

6.1 Conclusion

In this work the behavior of total water storage along with other water cycle component in Ob river basin since 2003 are discussed. The equivalent water height is through GRACE and GRACE-FO mission determined, precipitation and evapotranspiration are obtained from various data models and runoff is measured using satellite altimetry. For each of these component, one final time series is generated using mathematical and statistic methods. The whole time series divide into 3 periods and the change of each component in these periods are analyzed.

The GRACE data showed that before 2013, the total water storage in Ob river basin has slightly decreased by 0.68 ± 0.25 mm/month, from 2013 to 2015 there is a positive trend of the total water storage (3.31 ± 0.86 mm/month) and this is due to the growth of the precipitation amount (39.12 ± 0.35 to 44.32 ± 0.64 mm/month). After 2015, the precipitation in this area has a decline comparing to the value between 2013 and 2015 (41.28 ± 0.55 mm/month). Though evapotranspiration are also weaker in this period the reduction was not as strong as precipitation and meanwhile runoff may have increased. As a result, total water storage has reduced by 0.80 ± 0.57 mm/month since 2016.

The water increase from 2013 to 2015 happened in north west of this catchment. The water lost after 2016, however, took place not only in north west, but also in south east.

6.2 Outlook

There is still some questions that can be answered. We've already found the difference of water storage change in different subareas, by further spatial analyzing the water behavior of different subareas can be analyzed. Furthermore, water storage exists in different forms like groundwater recharge and permafrost, the hydrological implications of continued permafrost degradation is complicated in high-latitude regions [28]. Further research is needed in order to understand the water behavior.

Bibliography

- [1] Overview - monthly mass grids.
- [2] Richard G Allen, Luis S Pereira, Dirk Raes, Martin Smith, et al. Crop evapotranspiration-guidelines for computing crop water requirements-fao irrigation and drainage paper 56. *Fao, Rome*, 300(9):D05109, 1998.
- [3] Mingyue Chen, Pingping Xie, John E Janowiak, and Phillip A Arkin. Global land precipitation: A 50-yr monthly analysis based on gauge observations. *Journal of Hydrometeorology*, 3(3):249–266, 2002.
- [4] heather Doyle. What is permafrost. 2020.
- [5] H. E. Dregne. Salinization of land and water resources. *Soil Science*, 161(2):137–138, feb 1996.
- [6] Terry E Evans. The effects of changes in the world hydrological cycle on availability of water resources. *Global Climate Change and Agricultural Production: Direct and Indirect Effects of Changing Hydrological, Pedological and Plant Physiological Processes*, pages 15–48, 1996.
- [7] Karen E. Frey and James W. McClelland. Impacts of permafrost degradation on arctic river biogeochemistry. *Hydrological Processes*, 23(1):169–182, jan 2009.
- [8] Peter H Gleick. Water in crisis. *Pacific Institute for Studies in Dev., Environment & Security. Stockholm Env. Institute, Oxford Univ. Press. 473p*, 9, 1993.
- [9] Dazhong Han and John Wahr. The viscoelastic relaxation of a realistically stratified earth, and a further analysis of postglacial rebound. *Geophysical Journal International*, 120(2):287–311, feb 1995.
- [10] Hans Hersbach, Bill Bell, Paul Berrisford, Shoji Hirahara, András Horányi, Joaquín Muñoz-Sabater, Julien Nicolas, Carole Peubey, Raluca Radu, Dinand Schepers, et al. The era5 global reanalysis. *Quarterly Journal of the Royal Meteorological Society*, 146(730):1999–2049, 2020.
- [11] Eugenia Kalnay, Masao Kanamitsu, Robert Kistler, William Collins, Dennis Deaven, Lev Gandin, Mark Iredell, Suranjana Saha, Glenn White, John Woollen, et al. The ncep/n-car 40-year reanalysis project. *Bulletin of the American meteorological Society*, 77(3):437–472, 1996.
- [12] C. Kidd. Satellite rainfall climatology: a review. *International Journal of Climatology*, 21(9):1041–1066, 2001.
- [13] Philip P. Micklin Liliya Konstantinovna Malik, Lewis Owen. Ob river.
- [14] Christof Lorenz, Harald Kunstmann, Balaji Devaraju, Mohammad J Tourian, Nico Sneeuw, and Johannes Rieger. Large-scale runoff from landmasses: a global assessment

- of the closure of the hydrological and atmospheric water balances. *Journal of Hydrometeorology*, 15(6):2111–2139, 2014.
- [15] NASA. Grace mission. https://www.nasa.gov/mission_pages/Grace/spacecraft/index.html.
- [16] Philip Gbenro Oguntunde. *Evapotranspiration and complimentarity relations in the water balance of the Volta Basin: Field measurements and GIS-based regional estimates*. Cuvillier, 2004.
- [17] M. C. Peel, B. L. Finlayson, and T. A. McMahon. Updated world map of the koeppen-geiger climate classification. *Hydrology and Earth System Sciences*, 11(5):1633–1644, oct 2007.
- [18] C. Revenga, World Resources Institute, S. Murray, A. Hammond, and J.N. Abramovitz. *Watersheds of the World: Ecological Value and Vulnerability*. World Resources Institute report. World Resources Institute, 1998.
- [19] M. Rodell, J. S. Famiglietti, D. N. Wiese, J. T. Reager, H. K. Beaudoin, F. W. Landerer, and M.-H. Lo. Emerging trends in global freshwater availability. *Nature*, 557(7707):651–659, may 2018.
- [20] Himanshu Save, Srinivas Bettadpur, and Byron D. Tapley. High-resolution CSR GRACE RL05 mascons. *Journal of Geophysical Research: Solid Earth*, 121(10):7547–7569, oct 2016.
- [21] Qiaohong Sun, Chiyuan Miao, Qingyun Duan, Hamed Ashouri, Soroosh Sorooshian, and Kuo-Lin Hsu. A review of global precipitation data sets: Data sources, estimation, and intercomparisons. *Reviews of Geophysics*, 56(1):79–107, jan 2018.
- [22] B. D. Tapley. GRACE measurements of mass variability in the earth system. *Science*, 305(5683):503–505, jul 2004.
- [23] M. J. Tourian, N. Sneeuw, and A. Bárdossy. A quantile function approach to discharge estimation from satellite altimetry (ENVISAT). *Water Resources Research*, 49(7):4174–4186, jul 2013.
- [24] John Wahr, Mery Molenaar, and Frank Bryan. Time variability of the earth’s gravity field: Hydrological and oceanic effects and their possible detection using grace. *Journal of Geophysical Research: Solid Earth*, 103(B12):30205–30229, 1998.
- [25] Michael M Watkins, David N Wiese, Dah-Ning Yuan, Carmen Boening, and Felix W Landerer. Improved methods for observing earth’s time variable mass distribution with grace using spherical cap mascons. *Journal of Geophysical Research: Solid Earth*, 120(4):2648–2671, 2015.
- [26] Pingping Xie, M Chen, and W Shi. Cpc unified gauge-based analysis of global daily precipitation. In *Preprints, 24th Conf. on Hydrology, Atlanta, GA, Amer. Meteor. Soc*, volume 2, 2010.
- [27] Pingping Xie, Mingyue Chen, Song Yang, Akiyo Yatagai, Tadahiro Hayasaka, Yoshihiro Fukushima, and Changming Liu. A gauge-based analysis of daily precipitation over east asia. *Journal of Hydrometeorology*, 8(3):607–626, jun 2007.
- [28] N. L. Young, J.-M. Lemieux, H. Delottier, R. Fortier, and P. Fortier. A conceptual model for anticipating the impact of landscape evolution on groundwater recharge in degrading permafrost environments. *Geophysical Research Letters*, 47(11), jun 2020.

Appendix A

Estimating TWS from GRACE SH

The shape of the geoid, i.e. the distance between the reference ellipsoid and the geoid surface N , can be expanded in a sum of spherical harmonics.

$$N(\theta, \lambda) = R \sum_{l=0}^{\infty} \sum_{m=0}^l \tilde{P}_{lm}(\cos \theta) (\tilde{C}_{lm} \cos m\lambda + \tilde{S}_{lm} \sin m\lambda) \quad (\text{A.1})$$

where The time-dependent change in the geoid heights ΔN is reflected by the difference be-

- $N(\theta, \lambda)$ geoid height at a point with the spherical coordinates θ, λ
- R radius of the Earth
- \tilde{P}_{lm} normalized associated Legendre functions of degree l and order m
- $\tilde{C}_{lm}, \tilde{S}_{lm}$ normalized Stokes coefficients

tween the spherical harmonic coefficients $\tilde{C}_{lm}, \tilde{S}_{lm}$. In this case, the equation can be written as:

$$\Delta N(\theta, \lambda) = R \sum_{l=0}^{\infty} \sum_{m=0}^l \tilde{P}_{lm}(\cos \theta) (\Delta \tilde{C}_{lm} \cos m\lambda + \Delta \tilde{S}_{lm} \sin m\lambda) \quad (\text{A.2})$$

By assuming that $\Delta N(\theta, \lambda; t) \neq 0$, it is clear that there had to be a change in the Earth's gravity field caused by mass fluctuations in, on and above the Earth's surface. This change is denoted as a change in the Earth's density distribution. In[24], it was found that there is a connection between this quantity and its representation in spherical harmonic coefficients.

$$\left\{ \begin{array}{c} \Delta \tilde{C}_{lm}(t) \\ \Delta \tilde{S}_{lm}(t) \end{array} \right\} = \frac{3}{4\pi R \rho_{ave} (2l+1)} \int \int \Delta \rho(r, \theta, \lambda; t) \tilde{P}_{lm}(\cos \theta) \times \left(\frac{r}{R} \right)^{l+2} \left\{ \begin{array}{c} \cos m\lambda \\ \sin m\lambda \end{array} \right\} \sin \theta d\theta d\lambda \quad (\text{A.3})$$

where r is the distance of the computation point from the center of the Earth and ρ_{ave} is the average density of the Earth. However, an accurate determination of $\Delta \rho(r, \theta, \lambda; t)$ is nearly impossible, because it requires prior knowledge about the inner density distribution of the Earth. But all short periodic mass variations can be assumed to happen only in a thin layer on the Earth's surface, which can be detected by GRACE satellites. The thickness is mostly determined by the thickness of the atmosphere and is of the order of 10 to 15 km [24].

The change in this thick layer is called surface density $\Delta \rho_s$, which can be defined as the radial integral of $\Delta \rho$ through this layer and since the layer is thick enough, it can be assumed that $r \approx R$, so the equation can be simplified as

$$\left\{ \begin{array}{c} \Delta \tilde{C}_{lm}(t) \\ \Delta \tilde{S}_{lm}(t) \end{array} \right\}_{\text{surf mass}} = \frac{3}{4\pi R \rho_{ave} (2l+1)} \int \int \Delta \rho(\theta, \lambda; t) \tilde{P}_{lm}(\cos \theta) \left\{ \begin{array}{c} \cos m\lambda \\ \sin m\lambda \end{array} \right\} \sin \theta d\theta d\lambda \quad (\text{A.4})$$

This equation now connects the density redistribution in this thin layer with the spherical harmonic coefficients. Thus, it describes the contribution to the geoid from the direct gravitational attraction of the surface mass [24]. The mass fluctuations on the surface also deform the underlying Earth, which implicates a change in the gravitational potential, and thus a change in the geoid shape, as well. This effect is considered by the so called *Love number* k_l , which were derived from[9]. The contribution from the deformed solid earth may then be written as

$$\left\{ \begin{array}{l} \Delta \tilde{C}_{lm}(t) \\ \Delta \tilde{S}_{lm}(t) \end{array} \right\}_{\text{solid Earth}} = \frac{3k_l}{4\pi R\rho_{ave}(2l+1)} \int \int \Delta\rho(\theta, \lambda; t) \tilde{P}_{lm}(\cos\theta) \left\{ \begin{array}{l} \cos m\lambda \\ \sin m\lambda \end{array} \right\} \sin\theta d\theta d\lambda \quad (\text{A.5})$$

The total geoid change is obtained by adding (3.4) and (3.5)

$$\left\{ \begin{array}{l} \Delta \tilde{C}_{lm}(t) \\ \Delta \tilde{S}_{lm}(t) \end{array} \right\} = \left\{ \begin{array}{l} \Delta \tilde{C}_{lm}(t) \\ \Delta \tilde{S}_{lm}(t) \end{array} \right\}_{\text{surf Earth}} + \left\{ \begin{array}{l} \Delta \tilde{C}_{lm}(t) \\ \Delta \tilde{S}_{lm}(t) \end{array} \right\}_{\text{solid Earth}} \quad (\text{A.6})$$

Inserting (3.6) into (3.2) leads to the so called *isotropic transfer coefficients*, which define the quantity of a spherical harmonic series expansion. In the case of a surface mass density, they are defined as

$$\Lambda_l = \frac{R\rho_{ave}}{3} \frac{2l+1}{1+k_l} \quad (\text{A.7})$$

Then an expression for the surface mass density in terms of the spherical harmonic coefficients can be written as

$$\Delta\rho_S(\theta, \lambda) = \frac{R\rho_{ave}}{3} \sum_{l=0}^{\infty} \frac{2l+1}{1+k_l} \sum_{m=0}^l \tilde{P}_{lm}(\cos\theta) (\Delta\tilde{C} \cos m\lambda + \Delta\tilde{S} \sin m\lambda) \quad (\text{A.8})$$

The gravity field change can be assumed as the change of the thin layer of water on the Earth's surface. The relation between the water equivalent heights and the surface mass density is

$$h_W(\theta, \lambda) = \frac{\Delta\rho_S(\theta, \lambda)}{\rho_W} \quad (\text{A.9})$$

where ρ_W is the average density of water and thus

$$h_W(\theta, \lambda; t) = \frac{R\rho_{ave}}{3\rho_W} \sum_{l=0}^{\infty} \frac{2l+1}{1+k_l} \sum_{m=0}^l \tilde{P}_{lm}(\cos\theta) (\Delta\tilde{C} \cos m\lambda + \Delta\tilde{S} \sin m\lambda) \quad (\text{A.10})$$

For simplicity, this formula can be written as

$$h_W(\theta, \lambda; t) = \sum_{l=0}^{\infty} \Lambda_l \sum_{m=0}^l \tilde{Y}_{lm}(\theta, \lambda) \Delta\tilde{K}_{lm}(t) \quad (\text{A.11})$$

where

- $\Lambda_l = \frac{R\rho_{ave}}{3\rho_W} \frac{2l+1}{1+k_l}$: isotropic spectral transfer coefficients
- $\tilde{Y}_{lm}(\theta, \lambda) = \tilde{P}_{lm}(\cos\theta) (\cos m\lambda \quad \sin m\lambda)^T$: normalized surface spherical harmonics
- $\Delta\tilde{K}_{lm}(t) = (\Delta\tilde{C}_{lm} \quad \Delta\tilde{S}_{lm})^T$: normalized Stokes coefficients

The associated Legendre functions are given by

$$\tilde{P}_{n,m}(t) = \sqrt{(2 - \delta_{m0})(2n + 1) \frac{(n - m)!}{(n + m)!}} \sqrt{1 - t^2}^m \frac{d^{n+m}}{dt^{n+m}} \frac{1}{2^n n!} (t^2 - 1)^n \quad (\text{A.12})$$

where n is degree, m is order and $t = \cos \theta$ is a substitution. The Legendre functions can be calculated by the recursion.

$$\tilde{P}_{0,0}(t) = 1 \quad (\text{A.13})$$

$$\tilde{P}_{m,m}(t) = W_{m,m} \sin \theta \tilde{P}_{m-1,n-1}(t - 1) \quad \text{for } m > 0 \text{ and } m = n \quad (\text{A.14})$$

$$\tilde{P}_{n,m} = W_{n,m} [\cos \theta \tilde{P}_{n-1,m}(t) - \frac{1}{W_{n-1,m}} \tilde{P}_{n-2,m}(t)] \quad \text{for } m \neq n \quad (\text{A.15})$$

with the factors

$$W_{n,m} = \begin{cases} \sqrt{3} & \text{for } n = 1 \text{ and } m = 0, 1 \\ \sqrt{\frac{2n+1}{2n}} & \text{if } n = m \text{ and } n > 1 \\ \sqrt{\frac{(2n+1)(2n-1)}{(n+m)(n-m)}} & n > 1 \text{ and } m \neq n \end{cases} \quad (\text{A.16})$$

and the convention $\tilde{P}_{n,m}(t) = 0$ for $m > n$. This algorithm is shown to be stable until degree $n \approx 1800$. In this thesis they are up to 96.

It is obvious that only $\Delta \tilde{K}_{lm}$ is time dependent while Λ_l and $\tilde{Y}_{lm}(\theta, \lambda)$ are constant in time, by using the methods of forwards and backward-differences a rate of mass variations in terms of water equivalent heights can be obtained.

$$\dot{h}_W(\theta, \lambda; t) = \sum_{l=0}^{\infty} \Lambda_l \sum_{m=0}^l \tilde{Y}_{lm}(\theta, \lambda) \Delta \dot{\tilde{K}}_{lm}(t) \quad (\text{A.17})$$

This computation of the area weighted rate of change of water equivalent heights of one particular region χ , defined by a set of k grid cell centers $(\theta_i, \lambda_i), j = 1, 2, 3 \dots, k$, can be done according to

$$\dot{h}_W(\chi; t) = \sum_{j=1}^k \frac{a(\theta_i, \lambda_i)}{a(\chi)} \sum_{l=0}^{\infty} \Lambda_l \sum_{m=0}^l \tilde{Y}_{lm}(\theta_i, \lambda_i) \Delta \dot{\tilde{K}}_{lm}(t) \quad (\text{A.18})$$

In this thesis, the size of the cell is $0.5^\circ \times 0.5^\circ$, which means there are 360×720 cells. With

- $\dot{h}_W(\chi; t)$ rate of mass change in catchment χ
- k number of date points in the catchment
- $a(\theta_i, \lambda_i)$ area of the grid cell j
- $a(\chi)$ total area of the catchment χ

the help of the *shbundle*, *EWHbundle* and the basin mask from the Institute of Geodesy (GIS), University of Stuttgart, this process can easily be done and the equivalent water heights of Ob area between 2002 and 2020 are acquirable.